J. Fluid Mech. (2016), *vol.* 792, *pp.* 364–396. © Cambridge University Press 2016
doi:10.1017/jfm.2016.90

Combining an obstacle and electrically driven vortices to enhance heat transfer in a quasi-two-dimensional MHD duct flow

Ahmad H. A. Hamid[1,2], **Wisam K. Hussam**[1] **and Gregory J. Sheard**[1,†]

[1]The Sheard Lab, Department of Mechanical and Aerospace Engineering, Monash University, Victoria 3800, Australia

[2]Faculty of Mechanical Engineering, Universiti Teknologi MARA, 40450 Selangor, Malaysia

(Received 31 August 2015; revised 28 January 2016; accepted 29 January 2016; first published online 3 March 2016)

The design of vortex promoters in a heated-wall duct is often limited by the considerations of practicality, especially in complex systems such as fusion blankets. The present study investigates the use of current injection to invoke a street of vortices in quasi-two-dimensional high transverse magnetic field magnetohydrodynamic duct flows to enhance instability behind a cylinder. The intent is to generate intensive flow vorticity parallel to a magnetic field downstream of a field-aligned cylinder. Electric current enters the flow through an electrode embedded in one of the Hartmann walls, radiates outward, imparting a rotational forcing around the electrode due to the Lorentz force. The quasi-two-dimensional nature of these flows then promotes a vortical rotation across the interior of the duct with axis aligned to the magnetic field. The hot and cold walls are parallel to the magnetic field. Electric current amplitude and pulse width, excitation frequency and electrode position are systematically varied to explore their influences on the convective heat transport phenomenon. This investigation builds on a recommendation from previous work of Bühler (*J. Fluid Mech.*, vol. 326, 1996, pp. 125–150) dedicated to understanding of the flow stability in a similar configuration. This study provides supportive evidence for the use of current injection as an alternative to the conventional mechanically actuated turbuliser, with heat transfer almost doubled for negligible additional pumping power requirements.

Key words: high-Hartmann-number flows, magnetohydrodynamics, vortex shedding

1. Introduction

Magnetohydrodynamic (MHD) flows in rectangular ducts, amongst many other geometries, have received significant attention in the past due to their wide application (Shercliff 1953; Hunt 1965), especially in the cooling system of poloidal self-cooled blankets (Molokov 1994). It is known that magnetohydrodynamic effects serve to reduce the thermal hydraulic performance of these duct flows by greatly increasing the pressure drop and reducing the heat transfer coefficient through laminarisation of the flow (Hartmann & Lazarus 1937). An experimental investigation revealed that the

† Email address for correspondence: Greg.Sheard@monash.edu

transition to a laminar state occurs at $Re/Ha \approx 225$ (Brouillette & Lykoudis 1967), where $Ha = Ba\sqrt{\sigma/\rho\nu}$ is the Hartmann number and Re is the typical hydrodynamic Reynolds number. Here, B is the imposed magnetic field, a is the out-of-plane duct depth (in the magnetic field direction), while σ, ρ and ν are the electrical conductivity, density and kinematic viscosity of the liquid metal, respectively. The stabilizing effect derives from the additional damping in the form of Hartmann braking. In the limit of high magnetic field strength, a very thin boundary layer on the wall perpendicular to the magnetic field direction (known as the Hartmann layer) dominates the friction in an MHD duct flow (Krasnov, Zikanov & Boeck 2012) and the flow becomes quasi-two-dimensional (with 2-D core flow and 3-D flow confined in the boundary layers). In this regime, the induced currents predominantly reside in the Hartmann layer, and hence Joule dissipation is only important in this layer (Pothérat, Sommeria & Moreau 2000). Furthermore, in the context of fusion applications, liquid metals have a very high electrical conductivity ($\sigma = O(10^6)\ \Omega^{-1}\ \mathrm{m}^{-1}$; Lyon 1952), thus Joule dissipation becomes insignificant when compared to the high heat flux at the plasma-facing wall (Burr *et al.* 2000). In this case, Hartmann damping plays a greater role in the damping of the 2-D vortices (Mück *et al.* 2000). Substantial progress has been made using both experiments and modelling to understand these physical phenomena in various geometries relevant to the cooling ducts of liquid metal fusion blanket. Analytic solutions have been obtained in a number of simple geometries for both conducting and insulating ducts (Müller & Bühler 2001).

The cooling process can be assisted either by mixing of the flow via turbulence or vortical structures, or by the acceleration of a near-wall flow. The latter is encountered in MHD duct flows where the Hartmann walls are perfectly electrically conducting and the Shercliff walls are electrically insulating (known as Hunt's flow; Hunt 1965). In this configuration, high velocity jet flows near the sidewalls give rise to an M-shaped profile. It has been shown previously that an increase in magnetic field intensity generally leads to an improved heat transfer near the walls (Miyazaki *et al.* 1986; Cuevas *et al.* 1997; Takahashi *et al.* 1998).

In contrast, when all walls are insulating, the flow presents a flat velocity profile in the core region, monotonically decreasing to zero through the side layers. The flow in this configuration generally features a lower heat transfer from the heated sidewall as compared to the conducting Hartmann wall counterpart (Cuevas *et al.* 1997). It has been reported that the transverse magnetic field tends to inhibit the convective mechanism of heat transfer in an insulated duct flow by as much as 70 % (Gardner & Lykoudis 1971). Despite the low heat transfer characteristic, insulated ducts offer promising application to fusion blankets due to their low pressure drop (Cuevas *et al.* 1997). Hence it has become a particular interest of researchers to enhance the heat transfer in this flow configuration. Several methods have been proposed to improve the convective heat transfer, but generally the mechanism is the same: either by promoting turbulence or by generating vortical velocity fields in the flow in order to enhance transverse fluid mixing and to reduce thermal boundary layer thickness (Sukoriansky *et al.* 1989). Suggested methods to generate these vortices include placement of an obstacle such as a cylinder in the duct (Malang & Tillack 1995; Hussam & Sheard 2013), grid bars (Sukoriansky *et al.* 1989; Branover, Eidelman & Nagorny 1995) or a wall protrusion (Kolesnikov & Andreev 1997). However, the level of turbulence is dependent on the flow conditions. For example, high magnetic fields result in a low bulk flow velocity upstream of the obstacle, which then leads to a complete suppression of wake shedding downstream of the cylinder (Lahjomri, Capéran & Alemany 1993) or turbulence (Shatrov & Gerbeth 2010). In the case

of a cylinder obstacle, the kinematics of the wake vortices can be enhanced via an active excitation. Hussam, Thompson & Sheard (2012*b*) reported that the optimum perturbations leading to Kármán vortex shedding are localized in the near-wake region around the cylinder, which can be excited by a cylinder oscillation. Studies have examined cylinder rotation about its own axis (Beskok *et al.* 2012; Hussam, Thompson & Sheard 2012*a*), or oscillated in either a transverse direction (Yang 2003; Fu & Tong 2004; Celik, Raisee & Beskok 2010) or in line with the incident flow (Griffin & Ramberg 1976). The resulting vorticity field in all cases are similar, despite the different oscillation mechanisms (Beskok *et al.* 2012). It has been found that increasing oscillation amplitude leads to a higher convective heat transfer from a hot wall (Yang 2003; Beskok *et al.* 2012), though the gains become more modest at larger amplitudes (Hussam *et al.* 2012*a*). Furthermore, substantial improvement in Nusselt number has been observed when the cylinder oscillates with a frequency within the lock-in regime (Fu & Tong 2004), a region over which the cylinder motion governs the wake shedding frequency. An oscillation frequency beyond this lock-in regime leads to a lower convective heat transport (Yang 2003; Celik *et al.* 2010; Beskok *et al.* 2012). It is also found that higher oscillation amplitude leads to a lower optimum oscillation frequency (Hussam *et al.* 2012*a*) and broader primary lock-in regime (Mahfouz & Badr 2000).

In general, a remarkable heat transfer enhancement associated with active excitation has been reported. However, studies relevant to duct heat transfer enhancement in MHD flows are rather scarce. Furthermore, employing a mechanical actuator for such turbulisers in a duct faces significant technical obstacles to a practical implementation. An alternative vorticity generation mechanism is by the use of inhomogeneous wall conductivity, as has been explored by Bühler (1996). The smoothly transitioned wall conductance inhomogeneity leads to the formation of a quasi-2-D shear layer in the duct. Above a critical Reynolds number, which depends on Hartmann number, this shear layer is strong enough to trigger Kelvin–Helmoltz instabilities (Smolentsev, Vetcha & Moreau 2012), which result in the wake resembling that of Kármán vortex street. However, this mechanism acts passively on the flow and lacks a means to control the ensuing vorticity.

Alternatively, one can take advantage of the MHD flow characteristics, i.e. the presence of an imposed magnetic field in an electrically conducting flow, to intensify vortical structures by means of electric current injection from an electrode mounted flush with one of the Hartmann walls. The design and implementation of such a system would avoid the complexity of a mechanically actuated turbulence promoter system. Furthermore, the amount and rate of current injection can be actively controlled based on feedback from the flow conditions. Electrical generation of vortices has already been used to generate vortices parallel to the imposed magnetic field by Sommeria (1988), Pothérat, Sommeria & Moreau (2005), Pothérat & Klein (2014) in the study of decaying vortices, flow stability and MHD turbulence, but not yet in a duct arrangement with sidewall heating.

The aim of the present work is to enhance heat transfer from the heated sidewall of an MHD duct by utilizing a passive cylinder wake mechanism augmented with a current injection forcing. Influences of vortex dynamics on heat transfer, pressure drop and efficiency enhancement are examined over a wide range of current injection amplitudes, frequencies and pulse width, magnetic field strength, cylinder gap ratios and electrode positions. We focus on a flow with Reynolds number $200 \leqslant Re \leqslant 3000$ and friction parameter $200 \leqslant H = n(L/a)^2 Ha \leqslant 5000$ in a duct with a blockage ratio $\beta = d/2L = 0.2$, where n is the number of Hartmann walls ($n = 1$ in the case with

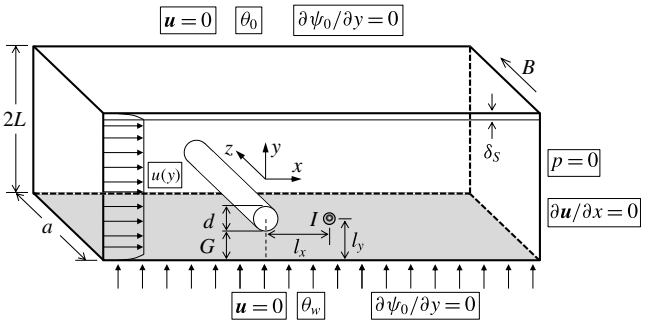

FIGURE 1. Schematic diagram of the system under investigation. The cylinder spans the duct, with diameter d and axis parallel to z-direction, and the small circle indicates a point electrode embedded in one of the Hartmann walls.

a free surface and $n=2$ for a flow between two Hartmann walls), L is half of the duct width and d is cylinder diameter. These parameters are chosen as they produce time periodic flows at each gap ratio, permitting investigation of the interaction between the forcing current injection and the natural vortex shedding behind the cylinder. Owing to the fact that there is a limited number of studies on actively excited cylinder wake vortices in an MHD duct flow in the literature, the present investigation will furnish valuable information for the design of efficient heat transport systems in high magnetic field applications.

This paper is organized as follows: the problem set-up and relevant equations are presented in § 2.1–2.3. A sensitivity study on numerical parameters concerning the grid independence and domain length are presented in § 2.4. In § 3, the results related to heat transfer enhancement are presented. Section 4 is dedicated to the analysis of pressure loss and overall efficiency of the system, followed by conclusions in § 5.

2. Methodology

2.1. *Computational set-up*

In this investigation a flow of electrically conducting fluid passing over a circular cylinder in a rectangular duct is considered (as depicted in figure 1). The bottom wall of the duct (grey shaded region in figure 1) is maintained at a constant hot temperature of θ_w, while the top wall and inflow have a constant cold temperature of θ_0. The cylinder is thermally insulated, while the duct sidewalls and the cylinder are each electrically insulated. On the duct walls and the cylinder surface, a no-slip condition is imposed. A fully developed quasi-2-D MHD duct flow is applied at the duct inlet (Pothérat 2007), defined by

$$u(y)=\frac{\cosh\sqrt{H}}{\cosh\sqrt{H}-1}\left(1-\frac{\cosh(\sqrt{H}y)}{\cosh\sqrt{H}}\right), \tag{2.1}$$

while at the outlet, a constant reference pressure is imposed and a zero streamwise gradient of velocity is weakly imposed. The transverse distance between the cylinder and the heated wall is characterised by the gap ratio G/d. This study considers gap ratios $G/d=0.5$, 1 and 2, with $G/d=2$ corresponding to the duct centreline. The wake flow is modified by means of current injection through an electrode embedded

at various locations in the otherwise electrically insulating out-of-plane duct wall. The ratio of cylinder diameter to the duct width (i.e. blockage ratio, $\beta = d/2L$) is fixed at 0.2 throughout this study. A uniform magnetic field B is imposed in the axial direction (z-axis).

In the present context, the magnetic Reynolds number Rm is low and hence the Lorentz force is diffusive in nature due to the typical low-velocity liquid metal and relatively small length scale (Davidson 2001). The fluctuating induced magnetic field around the externally applied field is negligible, and therefore, the quasi-static approximation is invoked (Roberts 1967). However, Alfvén waves might be generated when either the Hartmann number is sufficiently high or strong current pulses are injected into the flow. Their propagation along the magnetic field is governed by the Lundquist number $S = Ha\,Pr_m^{1/2}$ (Lundquist 1949), where Pr_m is the magnetic Prandtl number. For liquid metals, the quasi-static approximation holds when $Ha \leqslant O(10^3)$ (Pothérat & Kornet 2015). Taking this constraint into consideration, the magnetic field intensity was limited to $H = 5000$ (which corresponds to $Ha = 10^4$ for $n = 2$ and $\alpha = 1$). It should be noted that the bulk of the present numerical simulations was based on the flow at $H = 500$. Here, $\alpha = a/2L$ is the aspect ratio of the duct. It is therefore anticipated that the Alfvén waves, if present, will produce rather limited effects due to strong dissipation. Moreover, current pulses have been used previously to drive quasi-2-D flows (Sommeria 1988) and no such effect was reported.

For large interaction parameter, the flow tends towards two-dimensionality (Sommeria & Moreau 1982). Recent evidence of the quasi-two-dimensionality of MHD flows can be found in Krasnov *et al.* (2012), Kanaris, Albets, Grigoriadis & Kassinos (2013), Rhoads, Edlund & Ji (2014). A typical quasi-two-dimensional velocity profile is shown in figure 1, characterised by a flat profile in the core with velocity U_0 and high gradients in the vicinity of the lateral walls (Pothérat 2007).

2.2. *Governing equations*

In the present investigation, the flow is described by a theoretical model proposed by Sommeria & Moreau (1982) based on a quasi-2-D assumption where the flow quantities in the 2-D core flow and in the Hartmann layers are averaged along the magnetic field direction to give a modified two-dimensional Navier–Stokes equation augmented by a linear braking term representing friction in the Hartmann layers. This averaging is possible when the so-called two-dimensionalisation time $\hat{\tau}_{2D} = \rho\lambda^2/\sigma\hat{B}^2$, where $\lambda = l_\parallel/l_\perp$ is the ratio of the scales parallel and perpendicular to the magnetic field, i.e. the time for the Lorenz force to act to diffuse momentum of a fluid structure along magnetic field lines (Sommeria & Moreau 1982), is much shorter than any other time scales so that quasi-two-dimensionality is achieved within the flow. The relevant time scales include the time scales for viscous diffusion in both perpendicular and parallel planes, and the inertia time scale. These conditions are attained when both Hartmann number $Ha \gg 1$ and interaction parameter $N \gg 1$, in which any velocity variations along the magnetic field direction is suppressed almost instantaneously (Pothérat *et al.* 2000), and the Hartmann layer is laminar (Pothérat & Schweitzer 2011). Here, the interaction parameter is defined as $N = Ha^2/Re_L$.

Hartmann number and Reynolds number were varied with $200 \leqslant H \leqslant 5000$ and $1500 \leqslant Re \leqslant 3000$. These parameter ranges correspond to $50 \lesssim N \lesssim 67\,000$ for $n = 2$ and $\alpha = 1$, which justifies the employment of the SM82 model. Theoretically, the SM82 model is accurate to order $\max(Ha^{-1}, N^{-1})$ (Pothérat *et al.* 2005). In the case of rectangular duct flows, the SM82 model has been verified against three-dimensional

analytical solutions, where the local error in the velocity profile in the sidewall boundary layer is less than 10 % (Pothérat *et al.* 2000). Furthermore, 3-D simulations of MHD wakes behind a cylinder by Mück *et al.* (2000) verified the accuracy of the quasi-2-D model at high N and Ha. This result is further supported by more recent 3-D simulations by Kanaris *et al.* (2013), where at the highest Ha investigated, they found maximum errors of the averaged parameters between the quasi-2-D model and the 3-D DNS of 6 % and 8 % for the steady and time-dependent flows, respectively. The model has also been found to predict the rate of decay of cylinder wake vortices very well within the high-N regime (Hamid *et al.* 2015). It is also worth mentioning that a quasi-2-D model proposed by Smolentsev & Moreau (2007) for MHD turbulence based on SM82 has been found to be in excellent agreement with previous experimental results.

Introducing the non-dimensional variables and coordinates which are defined from physical variables as

$$\left.\begin{gathered} p=\frac{1}{\rho {U_0}^2}\hat{p}, \quad \boldsymbol{x}=\frac{1}{L}\hat{\boldsymbol{x}}, \quad \theta=\frac{\hat{\theta}-\hat{\theta}_0}{\hat{\theta}_w-\hat{\theta}_0}, \\ \boldsymbol{u}=\frac{1}{U_0}\hat{\boldsymbol{u}}, \quad t=\frac{U_0}{L}\hat{t}, \end{gathered}\right\} \tag{2.2}$$

the non-dimensional MHD equations of continuity, momentum and energy are

$$\nabla\cdot\boldsymbol{u}=0, \tag{2.3}$$

$$\frac{\partial \boldsymbol{u}}{\partial t}=-(\boldsymbol{u}\cdot\nabla)\boldsymbol{u}-\nabla p+\frac{1}{Re_L}\nabla^2\boldsymbol{u}+\frac{L^2}{a^2}\frac{Ha}{Re_L}(\boldsymbol{u}_0-n\boldsymbol{u}), \tag{2.4}$$

and

$$\frac{\partial \theta}{\partial t}+(\boldsymbol{u}\cdot\nabla)\theta=\frac{1}{Pe}\nabla^2\theta, \tag{2.5}$$

respectively, where $\boldsymbol{u}$, p, θ and $\boldsymbol{u}_0$ are the velocity, pressure, temperature and forcing velocity field (which in the context of the present study, is a transverse electric current density imposed at the sidewalls), respectively, projected onto a plane orthogonal to the magnetic field, U_0 is peak inlet velocity and ∇ is the gradient operator. The dimensionless parameters Reynolds number Re_L, Hartmann number Ha and Peclet number Pe are defined as

$$\left.\begin{aligned} Re_L &= U_0 L/\nu, \\ Ha &= Ba\sqrt{\sigma/\rho\nu}, \\ Pe &= U_0 L/\kappa_T = Re_L Pr, \end{aligned}\right\} \tag{2.6}$$

where κ_T is the thermal diffusivity of the fluid. Prandtl number $Pr=\nu/\kappa_T$ characterizes the ratio of viscous to thermal diffusion in the fluid and $Pr=0.022$ is used throughout, representative of the eutectic alloy GaInSn. This liquid metal has been employed widely in MHD laboratory experiments, e.g. Frank, Barleon & Müller (2001), Morley *et al.* (2008), Klein, Pothérat & Alferenok (2009). In this paper, Hartmann number is expressed in term of a friction parameter $H=n(L/a)^2Ha$, following Pothérat (2007).

The electric current is injected in alternating-sign pulses with amplitude I and angular frequency $\omega_f=2\pi f_f$, where f_f is the forcing frequency, and pulse width,

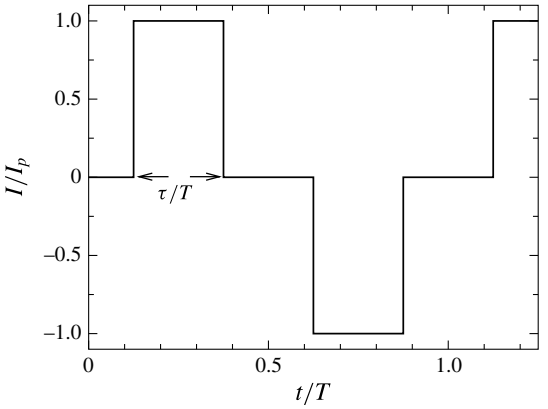

FIGURE 2. Typical electric current injection profile, represented by a modified square waveform with pulse width $0 < \tau/T < 0.5$. In the limit of $\tau/T = 0.5$, the current injection profile takes a square waveform. The amplitude of current is normalized by its peak amplitude, I_p, and the time is normalized by signal period, T.

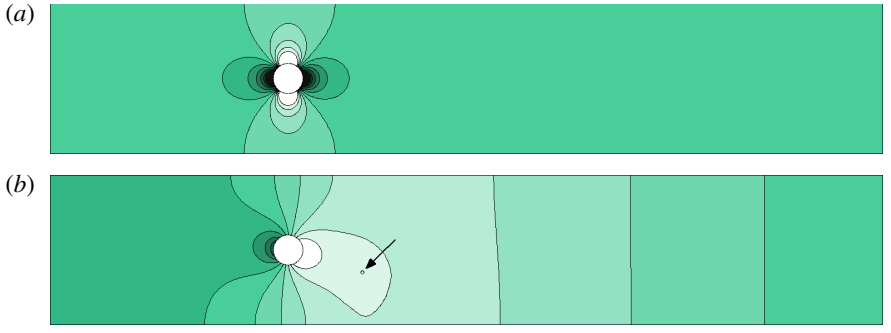

FIGURE 3. (Colour online) Contour plots of the difference in electrical potential field calculated from the analytical solution and the field that is solved numerically in the presence of the electrically insulating cylinder. In (*a*), current is injected from the base of the cylinder and contour levels range between -0.001 and 0.001, and in (*b*), current is injected from an electrode placed at $l_x = 1$ and $l_y = 0.7$ (indicated by the arrow), and contour levels range between -0.04 and 0.06. Light and dark contours represent positive and negative difference in electrical potential, respectively.

τ/T, where $T = 2\pi/\omega_f$ is the period of the current oscillation (ref. figure 2). For the analytical derivation of the forcing velocity fields, see appendix A. It is noted that these solutions are obtained for a duct with no cylinder present. While the cylinder diameter is small relative to the duct width, it is not negligible, and so this forcing solution inexactly approximates the true forcing field. In order to justify the validity of our solutions, we have evaluated the errors associated with the approximation by comparing the electrical potential field calculated from the analytical solution with the field that is solved numerically in the presence of the electrically insulating cylinder.

The results (as shown in figure 3) revealed that the errors are isolated to the vicinity of the cylinder. For a case where the electrode is coincident with the cylinder, the largest discrepancies were three orders of magnitude below the overall variations in the electrical potential field within the domain. When the electrode was

positioned downstream of the cylinder, errors were again isolated to the vicinity of the cylinder, and were at least an order of magnitude below the overall field variations. It is therefore expected that the resulting electrically generated vortices will closely resemble the true vortices.

It is important to ensure that the time scale at which the current forcing is imposed is much larger than the two-dimensionalisation time so that the induced vortex shedding is quasi-two-dimensional and satisfies the SM82 model assumptions. The condition for the forcing time scale is justified as follows: in the present study, the forcing frequency is varied between $\omega_f = 0.5$ and 10, which corresponds to a non-dimensional forcing time scale between $\tau_f = 2\pi/\omega_f \approx 13$ and 0.6, respectively. Following the scalings used in this study, the non-dimensional two-dimensionalisation time is expressed as $\tau_{2D} = \hat{\tau}_{2D} U_0/L = \rho U_o \lambda^2/\sigma L \hat{B}^2$. For $H = 500$ (a friction parameter at which the highest forcing frequency is simulated in this study; low friction parameter and high forcing frequency impose demanding requirements for the time scales), and taking $n = 2$, $\alpha = 1$, and the properties of low melting point eutectic alloy $Ga^{68}In^{20}Sn^{12}$ at 20 °C (density $\rho = 6.3632 \times 10^3$ kg m^{-3}, electrical conductivity $\sigma = 3.30737 \times 10^6$ Ω^{-1} m^{-1} and kinematic viscosity $\nu = 3.4809 \times 10^{-7}$ m^2 s^{-1}; Lyon 1952), the imposed magnetic field is $B = Ha/a\sqrt{\rho\nu/\sigma} = 4H\alpha^2\sqrt{\rho\nu/\sigma}/(na) \approx 0.26$ T. Taking the typical bulk flow velocity in the blanket $U_0 = 0.015$ m s^{-1} (Smolentsev *et al.* 2010), $l_\perp = L$ and $l_\parallel = a$ so that $\lambda = 2$, along with the typical length scale for the fusion blanket application $a = 0.1$ m (Smolentsev *et al.* 2010), the two-dimensionalisation time is then $\tau_{2D} \approx 0.03$. This time scale is at least an order of magnitude smaller than the forcing time scale, which justifies the quasi-two-dimensionality assumption.

While the most demanding forcing case considered in this study has a time period approximately 20 times the two-dimensionalisation time, the square or modified square forcing current waveforms introduce higher frequencies that may not be resolvable under the SM82 model. For instance, a modified square waveform with $\tau/T = 0.25$ may be described by a Fourier series with coefficients of the form

$$\sum_{n=1}^{\infty} \frac{2}{n\pi} \left[\cos\left(\frac{n\pi}{4}\right) - \cos\left(\frac{3n\pi}{4}\right) \right]. \tag{2.7}$$

Even-numbered coefficients are identically zero, and it can be seen that the odd-numbered harmonic coefficients scale with $1/n$. It would be expected therefore that the SM82 model will resolve at least up to the 19th harmonic in the aforementioned most demanding current forcing case, or components of the pulse waveform with magnitudes down to approximately 5 % of the first Fourier mode. In order to evaluate the sensitivity of the resulting flow to the number of included modes in the Fourier series representation of the ideal modified square waveform, simulations were performed at $H = 500$, $Re_L = 1500$, $I = 60$, $\omega_f = 10$ and $\tau/T = 0.25$. The effect is quantified by the deviations of the flow parameters (time-averaged Nusselt number Nu, total drag coefficient C_D and integral of velocity magnitude throughout the domain $\mathscr{L}^2$) obtained with pulses represented by the truncated Fourier series from the ideal square waveform. The results are presented in table 1, which shows that the deviations are small (<1 %) even for a sinusoidal (single harmonic) approximation to the square wave, quickly becoming insignificant (<0.005 %) when including the first three or more non-zero harmonics (frequencies that are well within the valid range of the SM82 model). We therefore expect that no artefacts will be present in

Included harmonic	ε_{Nu}	ε_{C_D}	$\varepsilon_{\mathscr{L}^2}$
1st	0.0389	0.5790	0.0909
3rd	0.0031	0.0761	0.0087
5th	0.0031	0.0016	0.0027
7th	0.0024	0.0003	0.0016
9th	0.0023	0.0027	0.0017
11th	0.0024	0.0046	0.0015
13th	0.0029	0.0009	0.0015

TABLE 1. Percent absolute deviations as a function of number of the harmonic in the Fourier representation of the imposed current pulses. The deviations were calculated relative to the ideal modified square waveform with $\tau/T = 0.25$. 1st harmonic represents a perfect sinusoidal waveform, where all the energy in the current signal is contained at the fundamental frequency.

our solutions due to high-frequency components of the modified square wave current forcing violating the SM82 model.

It is also important to ensure that the electrically driven vortices are well resolved by the SM82 model, particularly their scale in the perpendicular plane, i.e. the vortex core. Here, the scale is defined as the radius of the electrode (Hunt & Malcolm 1968). The smallest quasi-2-D structure that can be satisfactorily resolved by the model arises from the condition that $\tau_{2D} \sim \tau_v{}^{\perp}$, which yields $l_\perp \sim a/\sqrt{Ha}$. The bulk of the present numerical simulations were based on the flow at $H = 500$, which corresponds to $Ha = 1000$ for $n = 2$ and $\alpha = 1$. This then yields the smallest resolved scale of $l_\perp \sim a/30$. For a typical duct length scale $a = O(10^{-1}$ m), the electrode size must be at least in the order of millimetres, which is typical in MHD experiments (Hunt & Malcolm 1968; Sommeria 1988). Furthermore, a recent finding by (Hamid *et al.* 2015) demonstrates the capability of the SM82 model in predicting the evolution of quasi-2-D vortices even at rather moderate interaction parameters (i.e. $N \approx 31$). For the sake of comparison, the interaction parameter is varied between $N = 50$ and 67 000 in the present investigation, and hence justifies the implementation of the SM82 model. We may therefore assert that the present results are representative of the actual physical behaviour, at least within the correct order of magnitude.

2.3. *Quantification of duct flows thermal hydraulic performance*

The instantaneous Nusselt number variation along the heated duct walls is quantified by

$$Nu_w(x, t) = \frac{2L}{\theta_f - \theta_w} \left.\frac{\partial \theta}{\partial y}\right|_{wall}, \tag{2.8}$$

where θ_f is the bulk fluid temperature, which is calculated using the velocity and temperature distribution as

$$\theta_f(x, t) = \int_{-L}^{L} u\theta \, \mathrm{d}y \Big/ \int_{-L}^{L} u \, \mathrm{d}y. \tag{2.9}$$

For a periodic flow, the instantaneous wall Nusselt number calculated from equation (2.8) is also periodic. The time-averaged local Nusselt number at each x-station is

represented by $\overline{Nu_x}(x)$. Integrating over the length of the heated bottom wall, L_w, gives the time-averaged Nusselt number

$$Nu = \frac{1}{L_w}\int_0^{L_w} \overline{Nu_x}(x)\,\mathrm{d}x. \tag{2.10}$$

To quantify the efficiency of the current injection on the heat transfer, the efficiency index is adopted (Walsh & Weinstein 1979), defined as

$$\eta = \frac{\mathrm{HR}}{\mathrm{PR}}, \tag{2.11}$$

where HR and PR are the heat transfer enhancement ratio and pressure penalty ratio, given respectively by $\mathrm{HR} = Nu/Nu_0$ and $\mathrm{PR} = \Delta P/\Delta P_0$. Nu_0 is the time-averaged Nusselt number of the heated region of the duct without any current injection and ΔP and ΔP_0 are the time-averaged pressure drop across the duct, with and without current injection, respectively (with the cylinder present).

2.4. *Solver validation and grid independence study*

The governing equations were solved using a high-order in-house solver employing a spectral element method for spatial discretisation and a third-order scheme based on backwards differentiation for time integration (Sheard 2011). The numerical system has previously been employed to study confined hydrodynamic flows (Neild *et al.* 2010), as well as the heat transfer of stationary and oscillating cylinders in a duct (Hussam & Sheard 2013; Hussam *et al.* 2012*a*; Cassells, Hussam & Sheard 2016). The implementation of the SM82 model within the solver was also validated in Hamid *et al.* (2015), where the spatial history of peak vorticity in a wake behind a cylinder computed using the present solver and published 3-D MHD simulation data were compared, and remarkable consistency were demonstrated.

Meshes were constructed consisting of four regions: two regions near the transverse walls, a core region and a region in the vicinity of the cylinder. Elements are concentrated near the walls and the cylinder (as shown in figure 4*a*) to resolve the expected high gradients in MHD flows (Pothérat, Sommeria & Moreau 2002) and to capture the crucial characteristics of the boundary layer (e.g. boundary layer separation) (Ali, Doolan & Wheatley 2009). The grid is also compressed in the horizontal direction towards the cylinder.

To test the domain independence of the meshes constructed for this study, the dependence of Nusselt number on downstream domain length was investigated. A case with $H = 500$, $Re_L = 1500$, $I = 60$, $\omega_f = 1.75$ and $\tau/T = 0.25$ was considered. The results are summarised in table 2, and the variation of time-averaged Nusselt number along the duct is given in figure 4(*b*). The result reveals that truncating the downstream length from $16L$ to $8L$ or $12L$ causes errors of less than 0.09 % or 0.08 %, respectively, in the time-averaged Nusselt number calculated up to $L_d = 8L$. Hence, the M1 mesh sizing was used hereafter.

A grid independence study was performed by varying the element polynomial degree, while keeping the macro-element distribution unchanged. The time-averaged Strouhal number $St = fd/U_0$, total drag coefficient $C_D = 2F_D/\rho U_0{}^2 d$, where F_D is the drag force exerted by the fluid per unit length of the cylinder, the integral of velocity magnitude throughout the domain ($\mathscr{L}^2$ norm) and Nusselt number (Nu) were monitored, as they are known to be sensitive to the domain size and resolution.

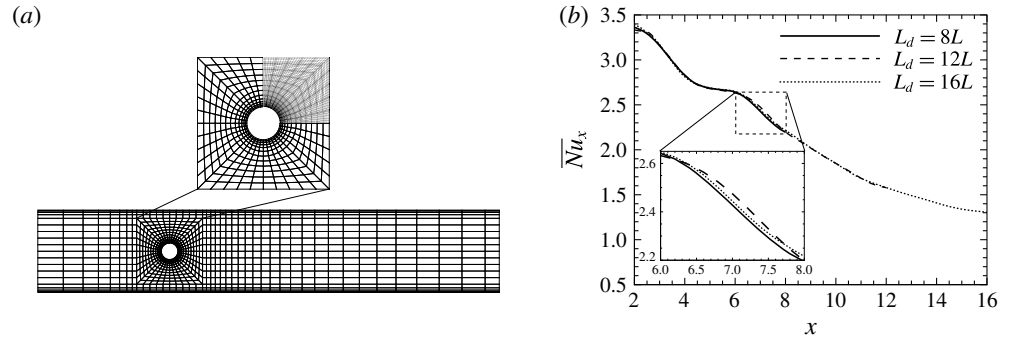

FIGURE 4. (*a*) Macro-element distribution of the computational domain, and magnified mesh in the vicinity of the cylinder, with the upper right quadrant representing the distribution of collocation points within elements with $N_p = 8$. The mesh extends $3.2L$ upstream and $8L$ downstream. (*b*) Time-averaged local Nusselt number in the downstream of cylinder for $H = 500$, $Re_L = 1500$, $I = 60$, $\omega_f = 1.75$ and $\tau/T = 0.25$. Solid, dashed and dotted lines represent domains with respective downstream lengths $L_d = 8L$, $12L$ and $16L$.

Mesh	M1	M2	M3
L_d/L	8	12	16
N_{el}	1292	1425	1558
ε_{Nu}	0.0822	0.0712	0

TABLE 2. Domain length L_d/L and number of elements N_{el} of different meshes. $\varepsilon_{Nu} = |1 - Nu_{Mi}/Nu_{M3}|$ is the error in time-averaged Nusselt number relative to the case with longest domain for $H = 500$, $Re_L = 1500$, $I = 60$, $\omega_f = 1.75$ and $\tau/T = 0.25$.

N_p	ε_{St}	ε_{C_D}	$\varepsilon_{\mathscr{L}^2}$	ε_{Nu}
3	0.2813	4.4134	0.5788	5.0943
4	0.4048	0.2138	0.0296	3.4334
5	0.3903	0.6136	0.1104	2.5580
6	0.2714	1.1087	0.1812	1.9540
7	0.2624	1.0248	0.1763	1.5904
8	0.1884	0.5990	0.1040	0.8984
9	0.1698	0.9263	0.1095	0.5187
10	0.0882	0.8289	0.0446	0.2656

TABLE 3. Percent uncertainties as a function of element polynomial degree arising from the grid independence study at $H = 500$, $Re_L = 1500$, $I = 60$, $\omega_f = 4$ and $\tau/T = 0.25$.

Errors relative to the case with highest resolution, $\varepsilon_P = |1 - P_{Ni}/P_{N=11}| \times 100\,\%$, were defined as a monitor for each case, where P is the monitored parameter. A demanding MHD case with $H = 500$, $Re_L = 1500$, $I = 60$, $\omega_f = 4$ and $\tau/T = 0.25$ was chosen for the test. The results are presented in table 3, and show rapid convergence with increasing polynomial order. The case with polynomial degree 8 achieved at worst a $0.9\,\%$ error, and is used hereafter.

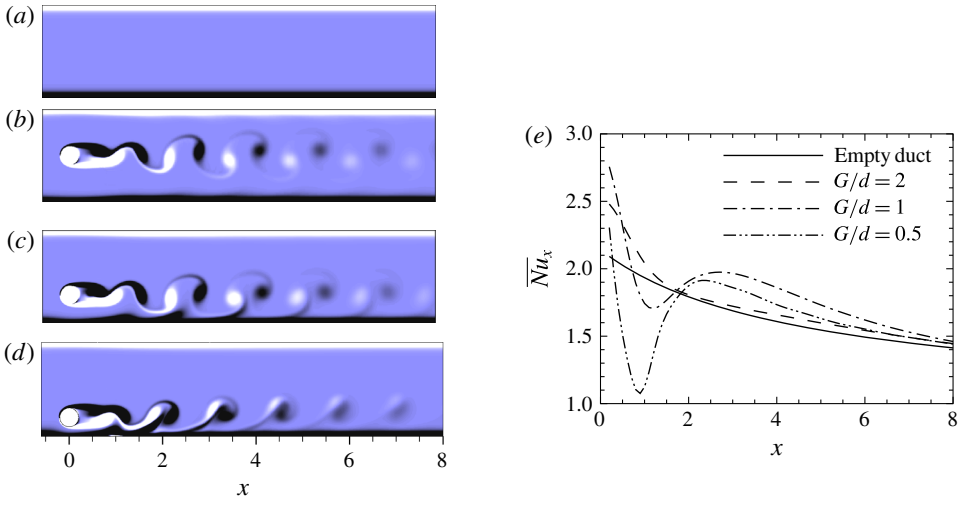

FIGURE 5. (Colour online) (*a–d*) Instantaneous vorticity contour plots and (*e*) time-averaged local Nusselt number in the downstream of cylinder. In (*a–d*), contour levels ranges between -2 and 2, with light and dark contours represent positive and negative vorticity, respectively. (*a*) Shows the case without a cylinder, while (*b–d*) respectively show cases $G/d = 2$, 1 and 0.5.

3. Results

3.1. *Base cases*

Three base cases, each having $Re_L = 1500$, $H = 500$ and $\beta = 0.2$, are constructed, with cylinder gap heights $G/d = 0.5$, 1 and 2, as well as a fourth case comprising the same duct but with the cylinder removed at the same flow conditions. The instantaneous vorticity contours for these cases are shown in figure 5, along with a plot of the streamwise distribution of the local time-averaged Nusselt number. With no cylinder, the flow is steady (see figure 5*a*) and the local Nusselt number decreases monotonically as the thermal boundary layer grows with distance from the inlet towards the fully developed value (see figure 5*e*). Figure 5(*b–d*) shows that the wall proximity affects the dynamics of the cylinder wake. Figure 5(*b*,*c*) illustrate a typical Kármán vortex shedding, whereas figure 5(*d*) shows a vortex pairing pattern in the wake. A strong entrainment of vorticity into the wake in the near-wake region occurs as the cylinder gap ratio is decreased, and this increases the local thermal boundary layer thickness (while temperature fields are not shown, they may be inferred from the vorticity field since they are correlated; Celik *et al.* 2010). This explains the abrupt decrease in local Nusselt number immediately downstream of the cylinder for the small gap ratio case, as shown in figure 5(*e*). This is then followed by an appreciable increase in Nusselt number due to the vortex shedding at the end of the formation region ($2 \lesssim x \lesssim 3$). Furthermore, when the cylinder is positioned at the centre of the duct, it was observed from figure 5(*b*) that the interaction between the wake and the walls is relatively weak, thus the trend of local Nusselt number resembles that of the empty duct case. The results of time-averaged Nusselt number along the heated wall reveal that cylinder placement with gap ratio $G/d = 1$ performed best, achieving heat transfer increment $HI = (Nu - Nu_e)/Nu_e = 8.6\,\%$, where Nu_e is the Nusselt number of an empty duct. This is followed by the case with $G/d = 2$

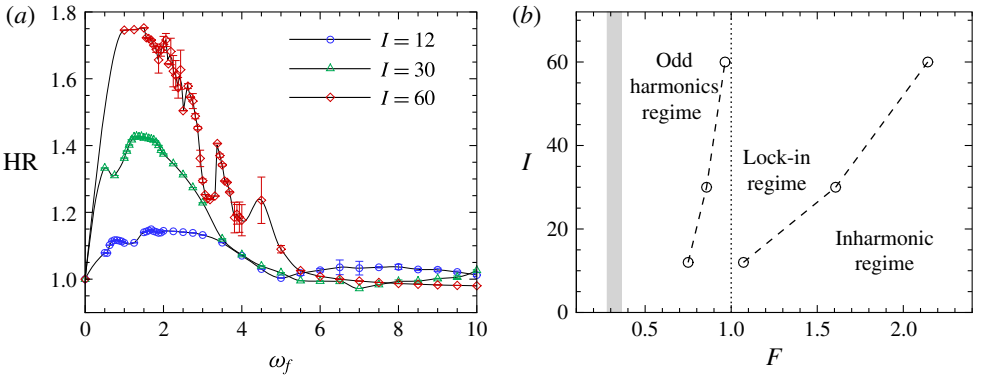

FIGURE 6. (Colour online) (*a*) Time-averaged heat transfer enhancement plotted against forcing frequency ω_f at non-dimensional current amplitudes I as indicated for $\tau/T = 0.25$ and $G/d = 2$. The current is injected from the cylinder. Error bars represent standard deviations of the mean Nusselt number within a shedding cycle evaluated at various shedding phases. (*b*) Limits of the lock-in regime as a function of forcing amplitude and normalized forcing frequency $F = f_f/f_0$. Regime to the left (right) of the lower (upper) bound represent wakes with odd harmonics (inharmonic) in cylinder lift force. The dotted line represent $F = f_f/f_0 = 1$, and the shaded region highlights the zone where HR is maximum.

G/d	Nu	ΔP	η	f_0
Empty duct	1.647	7.467	—	—
2	1.711	7.805	0.994	0.743
1	1.789	7.817	1.037	0.717
0.5	1.630	7.833	0.944	0.798

TABLE 4. Time-averaged flow quantities at $\beta = 0.2$, $H = 500$, $Re_L = 1500$ for the base cases.

($HI = 3.9\,\%$), and the poorest performance being the cylinder placed nearest to the wall with $G/d = 0.5$ ($HI = -1\,\%$). A similar trend is observed for the efficiency index (ref. table 4). This finding confirms a previous observation (Hussam & Sheard 2013), whereby an optimal gap between the cylinder and the heated wall for maximising the rate of heat transfer was found to lie within $0.8 \lesssim G/d \lesssim 1.4$. The trend of increasing pressure drop with increased gap ratio is also in agreement with the findings from that study.

3.2. *Effects of the current injection frequency and amplitude on heat transfer*

In this section, overall enhancement in heat transfer for various forcing frequency ω_f and forcing amplitude I are presented. The current is injected from the cylinder, and ω_f is varied between 0.5 and 10 for $I = 12$, 30 and 60. For all cases, $H = 500$, $\tau/T = 0.25$ and $G/d = 2$. The results are presented in figure 6(*a*). It can be observed that higher current amplitude leads to a higher peak heat transfer. Furthermore, HR reaches its maximum value at $1.3 \lesssim \omega_f \lesssim 1.7$, which corresponds to normalized forcing frequencies $0.28 \lesssim F = f_f/f_0 \lesssim 0.36$ within the investigated current amplitudes,

where f_0 is the natural shedding frequency. Spectral analysis of the cylinder lift coefficient $C_L = 2F_L/\rho U_0{}^2 d$, where F_L is the lift force exerted by the fluid per unit length of the cylinder, reveals that this frequency range is appreciably lower than the lock-in frequency range (a state where the vortex shedding is synchronised with the forcing frequency), as shown in figure 6(*b*). There are three distinct regimes of wake response, and further discussion on the frequency response analysis is presented in § 3.2.1. This observation contrasts previous studies of heat transfer from a heated channel wall in the presence of a cylinder oscillating either rotationally (Beskok *et al.* 2012) or transversely (Celik *et al.* 2010), where maximum heat transfer was observed at the lower range of the lock-in frequency. The observed discrepancy between the present results and the previous observations is attributed to the different mechanism of vorticity supply in both cases. In the oscillating cylinder case, the wake vortices are derived (or enhanced) through the relative motion between the cylinder and the free stream. This type of flow is governed by the relative size of the time scales of vortex dynamics and of cylinder oscillation. When the time scale of oscillation is comparable to that of vorticity, the vortex shedding is synchronised with the cylinder oscillation (the oscillation frequency is said to be in the lock-in regime). This leads to a generation of high intensity vortices and a substantial interaction between the vortices and the channel walls (Beskok *et al.* 2012). On the other hand, if the time scale of the oscillation is much smaller or much larger than the vortex dynamics (i.e. forcing frequencies outside the lock-in regime), the rate at which vorticity is shed into a wake is governed by the natural frequency irrespective of the oscillation frequency. The downstream wake in this state is similar to that for a fixed cylinder (Mahfouz & Badr 2000), and therefore inherit its poorer heat transfer characteristic.

In the present case, the wake vortices are governed by the forcing current injection, which is indicated by the presence of strong narrow peaks at the forcing frequency and its harmonics in the spectra of lift coefficient (which will be discussed further in § 3.2.1). For a low forcing frequency, the amount of vorticity supplied to each shed vortex is large, which leads to large wake vortical structure (as shown in figure 7). This in turn would generally enhance the wake–boundary layer interaction, and thus the heat transfer from the sidewall. However, a lower forcing frequency also means fewer shed vortices for a given time duration, which may not be beneficial for heat transfer enhancement. The competition between the size and number of shed vortices results in a non-monotonic trend in the HR–ω_f relation.

It is also interesting to observe that at higher forcing frequencies, the Nusselt number tends to asymptote towards the value obtained for the non-forced case (i.e. without current injection). Similar observations have been reported previously for a rotationally oscillating circular cylinder (Hussam *et al.* 2012*a*) and a transversely oscillating square cylinder (Yang 2003). This observation is attributed to the fact that for a high forcing frequency, the amount of vorticity feeding into the wake per shedding cycle decreases. This leads to a more coherent and smaller wake structure, resembling the unperturbed Kármán vortex shedding. The vortices therefore align closer to the duct centreline, which diminishes the interaction between wake vortices and thermal boundary layers (as can be seen in figure 7). Figure 6(*a*) shows for $I = 12$ a noticeable enhancement in heat transfer at higher forcing frequencies ($6 \lesssim \omega_f \lesssim 9$). The local Nusselt number variation along the duct was found to exhibit a relatively higher convective heat transfer further downstream of the cylinder at higher forcing frequency. This is generated by the enhanced wake–boundary layer interaction due to the development of vortex splitting in the downstream wake, as depicted in figure 8. The mechanism of this phenomenon is as follows: as an attached shear layer rolls

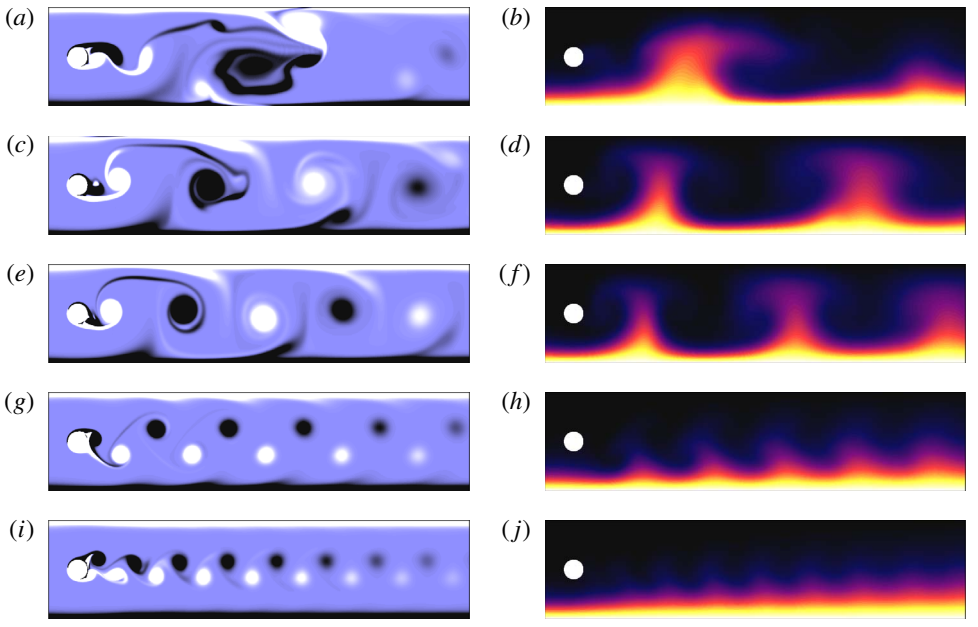

FIGURE 7. (Colour online) Contour plots of vorticity (*a*,*c*,*e*,*g*,*i*) and temperature (*b*,*d*,*f*,*h*,*j*) for current injection amplitude $I = 30$ and forcing frequencies $0.5 \leqslant \omega_f \leqslant 6$. Vorticity fields: contour levels are as per figure 5. Temperature fields: dark and light contours show cold and hot fluid, respectively. (*a*,*b*) $\omega_f = 0.5$, (*c*,*d*) 1.5, (*e*,*f*) 2, (*g*,*h*) 4, (*i*,*j*) 6.

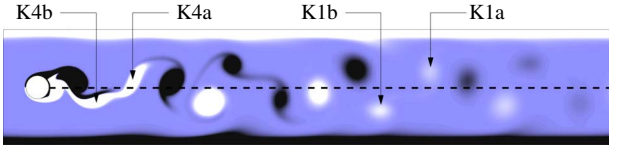

FIGURE 8. (Colour online) Instantaneous vorticity contour plots for $I = 12$ and $\omega_f = 6$. The dashed line represents the duct centreline. Contour levels ranges between -1 and 1, with light and dark contours represent positive and negative vorticity, respectively.

up halfway from the cylinder in the formation region, an incipient eddy of opposite sign crosses the wake centreline, causing the shear layer to stretch and finally split into two (i.e. vortices K1a and K1b) at approximately four diameters downstream of the cylinder. This process is repeated in the third successive phases (which results in the birth of vortices K4a and K4b), and the vortex sheds in the form of a regular Kármán vortex shedding between these two phases.

It is also worth mentioning that the fluctuations in the trend in Nusselt number for a higher forcing amplitude are due to the different modes of response of the wake at different forcing frequencies. For example, at $\omega_f = 3.375$, HR is 13 % higher than at $\omega_f = 3.3125$ for $I = 60$, despite the frequencies differing by less than 2 %. Vorticity and temperature contours for $\omega_f = 3.375$ (as shown in figure 9*a*,*b*) reveal that there is a substantial interaction between wake vortices and the heated wall due to the broadening of the width of the wake. There is clear evidence of boundary layer entrainment from the heated wall into the wake, as well as strong mixing between the

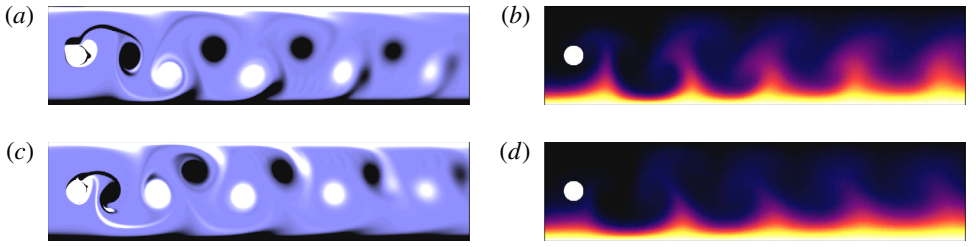

FIGURE 9. (Colour online) Instantaneous vorticity and temperature contour plots for $I = 60$ and (*a*,*b*) $\omega_f = 3.375$ and (*c*,*d*) $\omega_f = 3.3125$. Contour levels are as per figure 5. (*a*,*c*) Vorticity fields, (*b*,*d*) temperature fields.

high-temperature fluid near the heated region with the low-temperature core flow. In the case with $\omega_f = 3.3125$, however, almost no boundary layer entrainment from the heated wall into the wake was observed (as can be seen in figure 9*c*,*d*). This results in poor mixing between the hot fluid near the boundary and cold fluid in the core flow, which explains the abrupt increase in Nusselt number at this particular forcing frequency.

Inspection of instantaneous vorticity fields for these two frequencies reveals that the wakes are almost perfectly reflectively symmetric about the wake centreline. It has been shown previously that similar deflections of wake vortex shedding from the centreline is triggered by introducing local disturbances into the boundary layer on the cylinder by either heating the cylinder (Kieft *et al.* 2003) or rotating the cylinder (Lam 2009). In the present case, however, the current injection perturbation is in a modified square waveform with an alternating polarity, and therefore the boundary and forcing conditions are symmetrical about the duct centreline. To test the robustness of this bi-stable behaviour to asymmetry in the system, simulations were conducted with the cylinder shifted transversely by 5 % of the duct width, corresponding to $G/d = 2.25$ and $G/d = 1.75$. No clear trend concerning the cylinder position and the mode of wake response was found. The wake was biased upwards, downwards or was symmetric with respect to the duct centreline. The resulting heat transfer enhancement ratio data are presented in figure 10. For a given forcing frequency, HR was found to vary within a narrow range, indicated by the shaded region, due to the aforementioned uncertainty in the mode of wake response. Nevertheless, the overall trend remains: increasing forcing frequency leads to a lower heat transfer enhancement.

3.2.1. *Shedding frequency analysis*

In this section, Fourier analysis of the lift coefficient time histories and the vorticity time series are presented in order to investigate the response in the wake of the circular cylinder to the current injection. The analysis was conducted on data recorded after the transient start-up phase of the simulations had completed. The peaks in the resulting spectra are interpreted in terms of the natural shedding frequency, forcing frequency and their harmonics. The analysis reveals three distinct regimes of wake response: the odd harmonics regime, lock-in regime and inharmonic regime.

In the lock-in regime, the wake shedding frequency is governed only by the forcing current. In general, the synchronisation of vortex shedding (lock-in state) occurred over $0.8 < F < 2$ within the investigated forcing amplitude (ref. figure 6*b*). This compares quite well with the range of synchronisation $1.2 < F < 2.5$ for a circular cylinder oscillating in line with an incident flow of air observed by Griffin & Ramberg

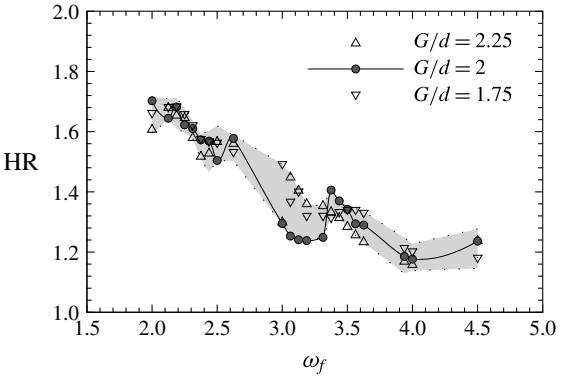

FIGURE 10. Time-averaged heat transfer enhancement plotted against forcing frequency for $I = 60$, $\tau/T = 0.25$, and ω_f and G/d as indicated. The current is injected from the cylinder. The shaded region highlights the zone bounded by $\max(\mathrm{HR} + \sigma_{HR})$ and $\min(\mathrm{HR} - \sigma_{HR})$, where σ_{HR} is the standard deviation of mean HR.

(1976). It should be noted that in the case of a transversely oscillating cylinder, a synchronisation range of $0.75 < F < 1.25$ was reported by Koopmann (1967). Despite these observed disparities, the qualitative trend is consistent: the domain of the lock-in regime increases with increasing forcing amplitude.

In the present cases, a distinct spectrum was observed outside the lock-in regime compared to the oscillating and vibrating cylinder cases. The typical lift force history is shown in figure 11(*a*), where the inharmonic case with $\omega_f = 1$ resembles a distorted waveform. When the forcing frequency is below the lock-in frequency threshold (i.e. in the region to the left of the lower bound shown in figure 6*b*), the spectrum is composed of the forcing frequency and its odd harmonics (as shown in figure 11(*c*) for $\omega_f = 1$), which corresponds to the forcing response. Beyond the lock-in regime (i.e. the inharmonic regime shown in figure 6*b*), the forcing frequency, its harmonic(s) and fraction of the natural shedding frequency (i.e. $f = nf_0/4$, where n are odd integers) are present in the spectrum (as shown in figure 11(*c*) for $\omega_f = 6$). The presence of multiple peaks may be the result of nonlinear interaction between the electrically generated vortices and the naturally shed vortices. Similar nonlinear interactions were reported by Karniadakis & Triantafyllou (1989) for a cylinder vibrating beyond the lock-in regime. Furthermore, the observed spectral peaks at frequencies lower than the forcing frequency can be explained by the aforementioned split vortex that misses the measurement 'probe' located at the duct centreline. It has previously been shown that only the natural shedding frequency or forcing frequency are dominant outside the lock-in regime for an oscillating cylinder (Celik *et al.* 2008), while only the natural shedding frequency is dominant outside the lock-in regime for a vibrating cylinder (Karniadakis & Triantafyllou 1989), although the presence of several other frequencies have been reported for some of these cases. Here, the spectrum in the lock-in regime is typical; the lift force fluctuation synchronises with the forcing frequency (shown by the strong narrow peak at $f/f_f = 1$ in figure 11(*c*) for $\omega_f = 3.5$) and with nearly uniform amplitude (as shown in figure 11*b*).

The wake response was further assessed via spectral analysis of the vorticity time series recorded at the duct centreline and at different streamwise positions (five, ten and fifteen diameters downstream of the cylinder, corresponding to $x = 2$, 4 and 6, respectively). It was found that, irrespective of the position where the

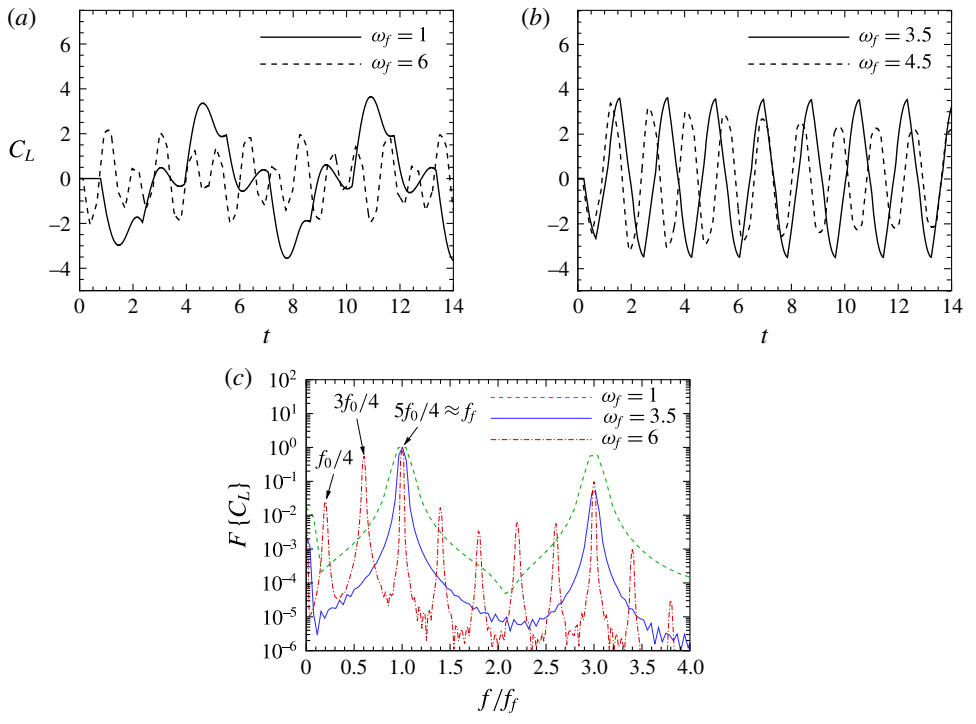

FIGURE 11. (Colour online) A typical time variation of the cylinder lift coefficient for $I = 12$ and ω_f as indicated within (*a*) unlock-in regimes and (*b*) lock-in regimes. (*c*) Respective Fourier spectra of the lift coefficient signals in (*a*) and (*b*).

signal was acquired, the wake exhibits a similar response (i.e. the spectrum peak is located at the same dominant frequency) for a given forcing amplitude and frequency. It was also observed that these signals have a similar response to the cylinder lift coefficient, except in the lock-in regime, where the frequency spectra exhibit peaks at odd harmonics. The appearance of these odd harmonic peaks in the spectrum is due to the absence of vorticity between two consecutive vortices of opposite sign, which results in an imperfect sinusoidal but symmetric waveform of vorticity time series (as shown in figure 12). For comparison, the corresponding cylinder lift coefficient time histories are shown in figure 11(*b*).

3.3. *Effects of the current injection amplitude and gap ratio on heat transfer*

This section examines the variation of HR with various forcing amplitude and at different transverse cylinder position. A typical plot is shown in figure 13. In general, HR increases with increasing forcing amplitude, with $\mathrm{HR}_{max} \approx 1.9$ across the computed parameters. The increment is relatively substantial compared to the gain observed for oscillating cylinder cases, e.g. in Hussam *et al.* (2012*a*), where $\mathrm{HR}_{max} \approx 1.2$ was reported for a case with maximum oscillation amplitude (i.e. $A = 3$), at optimum frequency, $Re_L \approx 1800$ and $H \approx 210$. It is noted that at a lower range of I (i.e. $I \lesssim 30$), the forcing current injection has a more profound effect on the heat transfer enhancement when the cylinder is placed closest to the heated side of the duct wall (i.e. $G/d = 0.5$) as compared to the other positions investigated. The reason for

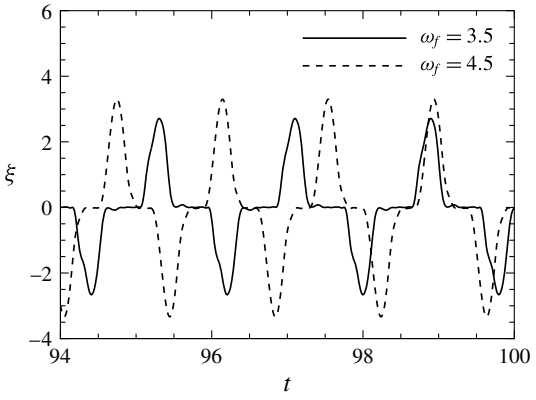

FIGURE 12. Time history of vorticity signal taken at $(x, y) = (0, 5d)$ for $I = 12$ and ω_f as indicated.

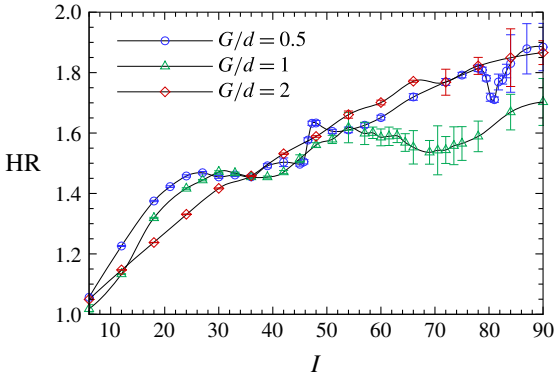

FIGURE 13. (Colour online) Heat transfer enhancement ratio plotted against current injection amplitude I at gap ratios G/d as indicated for $H = 500$, $\tau/T = 0.25$ and $\omega_f = 1.75$. The current is injected from the cylinder.

this is that when the cylinder is placed close to the wall, the shed vortices interact strongly with the thermal boundary layer in the vicinity of the cylinder, reducing its thickness and therefore increasing the local Nusselt number abruptly within the formation region (as shown by the sharp peak of the time-averaged local Nusselt number for the case of $G/d = 0.5$ and $I = 18$ in figure 14*a*). On the other hand, the interaction between the wake and the thermal boundary layer becomes weaker as the cylinder is placed further away from the wall, which results in relatively lower HR and more consistent local Nu along the duct (as shown by the almost uniform local Nu profile for the case of $G/d = 2$ and $I = 18$ in figure 14*a*).

However, for a large forcing amplitude, the duct with a cylinder placed on the centreline exhibits the highest enhancement in heat transfer. This occurs because for increasing I, the vortex becomes larger (as seen in figure 15*a–c*) and there is a consistently strong interaction between the heated wall and the cylinder wake along the duct. Furthermore, the local Nu is progressively increased over a downstream region up to $I = 54$ (as shown in figure 14*b*). Beyond $I = 54$, the local Nu exhibits a wavy pattern due to the complex interactions between the wake vortices and the

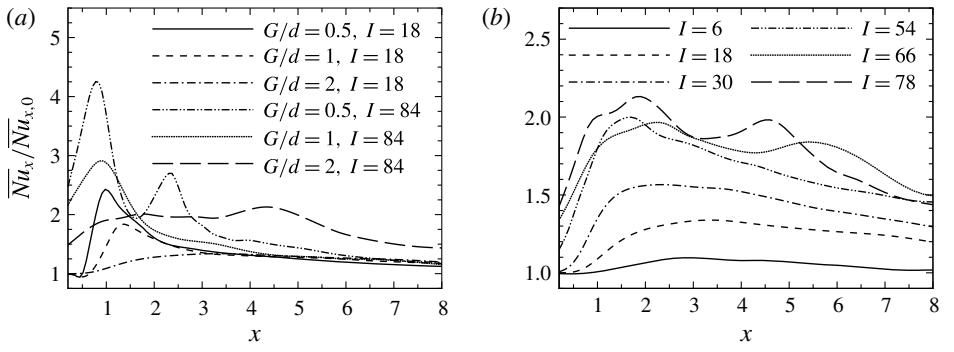

FIGURE 14. Normalized time-averaged local Nusselt number along the downstream of the heated wall for $\tau/T = 0.25$, $\omega_f = 1.75$ and (*a*) I and G/d as indicated, and (*b*) $G/d = 2$ and I as indicated.

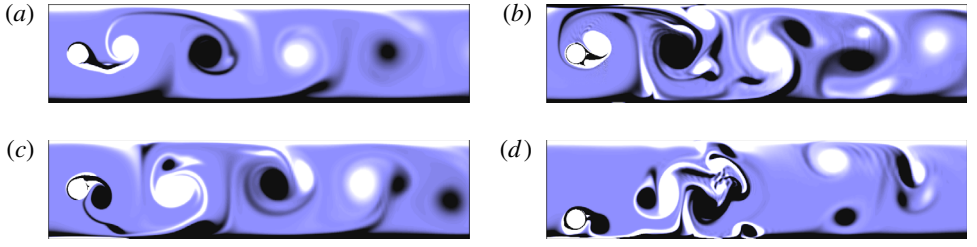

FIGURE 15. (Colour online) Instantaneous vorticity contour plots for (*a*) $I = 30$ and $G/d = 2$, (*c*) $I = 54$ and $G/d = 2$, (*b*) $I = 78$ and $G/d = 2$ and (*d*) $I = 84$ and $G/d = 0.5$. Contour levels are as per figure 5.

thermal boundary layer (as shown in figure 15*b*). Nevertheless, *Nu* increases steadily with I, as shown by the almost linear trend in the HR–I plot. For the asymmetric cases, on the other hand, the strong wake–boundary layer interaction remains only in the vicinity of the cylinder even for high I, which spans only approximately 20 % of the duct length, whereby a rapid decrease in local *Nu* downstream of the local maxima was observed (as shown in figure 14(*a*) for cases with $I = 84$). The reason for this observation is that the paired vortices are deflected away from the heated wall toward the opposite wall as they advect downstream (as shown in figure 15*d*).

Note also that the HR for cases with $G/d = 1$ tend to level off for $54 \lesssim I \lesssim 78$. A similar tendency was also observed for $G/d = 0.5$ cases, except that for $I \geqslant 60$, there is another relatively smaller peak of local Nusselt number downstream of the first one, as shown in figure 14(*a*) for $I = 84$. This second peak emerges due to the strong wall vorticity entrainment into the wake, induced by the paired vortices that have effectively shed (refer vorticity contours in figure 15*d*), and is attributed to the increase of HR with increasing I at a high forcing amplitude range. A similar observation was reported for transversely (Celik *et al.* 2010) and rotationally (Beskok *et al.* 2012) oscillating cylinders in duct arrangements, whereby the second peak of a local wall Nusselt number has a significant contribution to the spatial averaged heat transfer. It was also observed that as I increases, the magnitude of the second peak was increased and its distance from the cylinder was decreased.

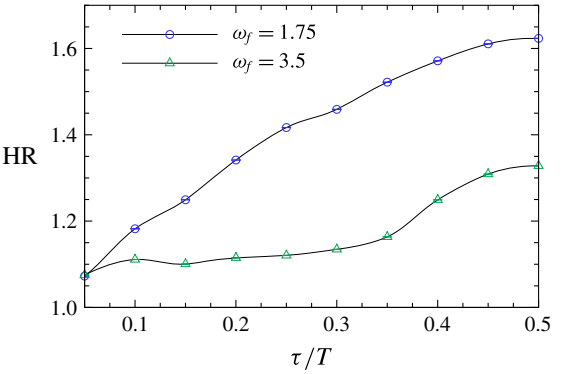

FIGURE 16. (Colour online) Heat transfer enhancement ratio plotted against current injection pulse width τ/T at frequencies ω_f as indicated for $H = 500$, $I = 30$ and $G/d = 2$. The current is injected from the cylinder.

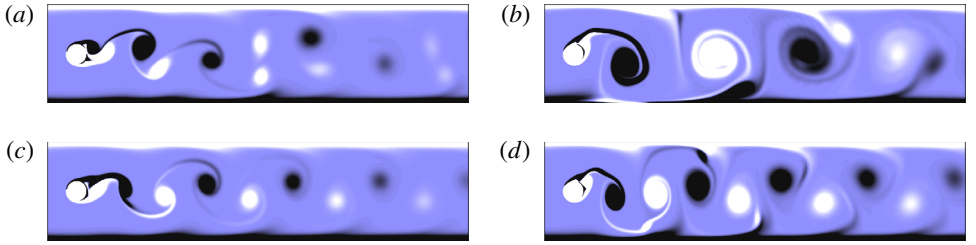

FIGURE 17. (Colour online) Instantaneous vorticity contour plots for $I = 30$ and (*a*) $\omega_f = 1.75$ and (*b*) $\omega_f = 3.5$. Contour levels are as per figure 5. (*a*,*c*) $\tau/T = 0.05$, (*b*,*d*) 0.5.

3.4. *Effects of the current injection pulse width and frequency on heat transfer*

Here the variation of Nusselt number with different forcing pulse width and frequency is examined. Figure 16 reveals that the heat transfer enhancement ratio increases monotonically with increasing forcing pulse width. This may be explained as for a given forcing frequency, the wake vortex size is larger for a longer forcing pulse width (as shown in figure 17). As a result, the wake–boundary layer interaction is enhanced, thinning the thermal boundary layer at the heated wall and thus improving the convective heat transport.

Furthermore, cases with $\omega_f = 1.75$ show a better heat transfer enhancement than the cases with $\omega_f = 3.5$. This observation is in agreement with the findings presented in § 3.2, where the Nusselt number reaches its maximum value at $1 \lesssim \omega_f \lesssim 2$ for $I = 30$. However, at the lowest forcing pulse width (i.e. $\tau/T = 0.05$), the enhancement in heat transfer is almost similar for both forcing frequencies. This is due to the fact that for low τ/T, the resultant wake vortices are relatively small, regardless of the forcing frequency. This in turn results in almost no interaction between the wake and the boundary layer (as shown in figure 17 for $\tau/T = 0.05$), which results in only an approximately 6 % enhancement in heat transfer.

For cases with $\tau/T = 0.5$, although the forcing current injection is in the form of a square wave (as shown in figure 2), the resulting wake resembles that of a Kármán vortex shedding, where there is a finite spacing between two consecutive shed vortices of opposite sign. This may be understood as follows: as the vortex rolls up, it is

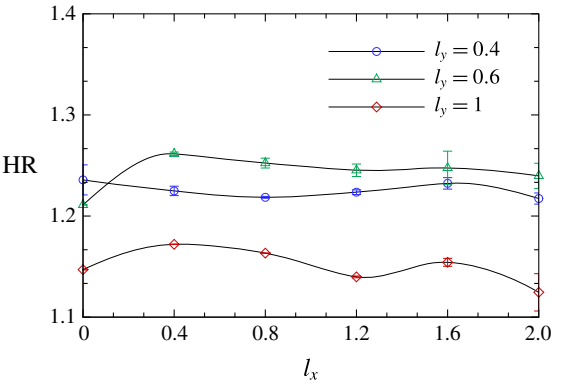

FIGURE 18. (Colour online) Heat transfer enhancement ratio plotted against horizontal distance l_x at vertical distance l_y as indicated for $I = 12$, $\omega_f = 1.75$, $\tau/T = 0.25$ and $G/d = 2$.

advected downstream and is effectively 'shed' before the forcing current switches to the opposite sign, forming a long tail that connects to the succeeding shed vortex of opposite sign (as can be seen in figure 17*b*,*d*). From these figures, it was also observed that the tail of the counter-clockwise (positive) vortices have a greater influence on thinning the thermal boundary layer than do the clockwise vortices. It is therefore anticipated that for a given pulse duty cycle D, the efficiency index may be further increased by injecting current which produces positive vorticity that has a longer pulse width relative to the negative vorticity. Here, $D = 2\tau/T$ for a modified square wave, which represents a fraction of one period in which the signal is active. This would be an interesting avenue for future study.

3.5. *Effects of the electrode position relative to the cylinder on heat transfer*

The effect of electrode position on the heat transfer enhancement ratio is demonstrated in figure 18. The electrode was placed at 18 different positions in the vicinity of the cylinder and the heated wall, in order to investigate the effect of complex interactions between the shear layers on the global heat transfer. Other parameters are fixed at $H = 500$, $I = 12$, $\omega_f = 1.75$, $\tau/T = 0.25$ and $G/d = 2$. The figure reveals that the enhancement in heat transfer is almost independent of the streamwise electrode position. The reason for this observation is due to the counterbalancing effect of the relative 'surplus' and 'deficit' in the local Nu (as depicted by the shaded regions in figure 19*a*); increased heat transfer downstream of the electrode as it is placed further downstream is offset by the larger region upstream of the electrode exhibiting low heat transfer. This happens because the heat transfer enhancement was observed to occur only at the downstream of the electrode (i.e. there was almost no enhancement at $x \lesssim l_x$), and due to the variations in the magnitude and/or location of the local Nu peaks with l_x.

Figure 18 also reveals that the heat transfer is significantly more sensitive to transverse electrode position. Inspection of the normalized local Nusselt number reveals that, for a given l_x, the peaks for cases with $l_y = 0.4$ are consistently higher than for the cases with $l_y = 0.6$ (as shown in figure 19*b*). The magnitude, however, decreased abruptly downstream of the electrode, due to the aforementioned deflection of shed vortices away from the heated wall toward the opposite wall for the offset

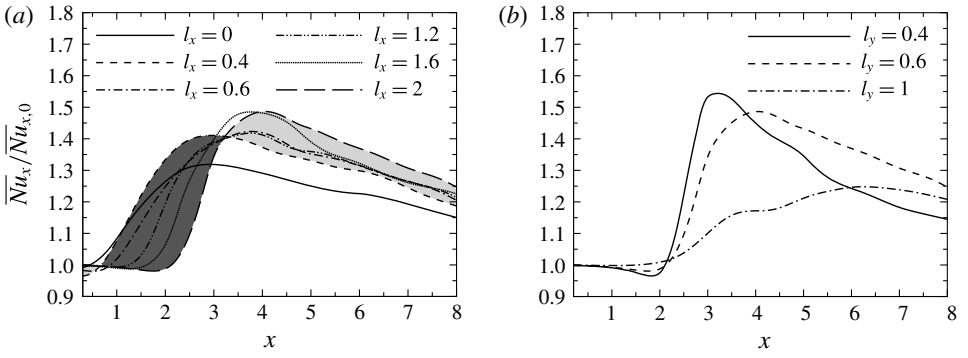

FIGURE 19. Normalized time-averaged local Nusselt number along the downstream of the heated wall. (*a*) The electrode is placed at $l_y = 0.6$ and at l_x as indicated. The dark (lighter) region correspond to a deficit (surplus) in heat transfer enhancement of case with $l_x = 2$ relative to the case with $l_x = 0.4$. (*b*) The electrode is placed at $l_x = 2$ and at l_y as indicated.

cylinder cases. This leads to a lower overall heat transfer enhancement than for cases with electrode placed at $l_y = 0.6$.

For a given l_y, the magnitude of the peaks were almost invariant with respect to l_x (with the coefficient of variation, $0.015 \leqslant CV \leqslant 0.046$ for all l_x), indicating that the magnitude of the peaks is governed by the electrode–wall proximity. However, at $l_y = 0.6$, the peak of time-averaged $Nu_x/Nu_{x,0}$ for $l_x = 0$ is significantly lower than the peaks for other l_x (as can be seen in figure 19*a*), which results in HR lower than the case for $l_y = 0.4$ for the same l_x (as shown in figure 18). This observation is consistent with the results presented in figure 13, where at a lower range of I, HR is higher when the cylinder is placed closest to the heated wall.

For the cases with electrode placed at the duct centreline, the wake–boundary layer interaction is weak throughout the duct, and there were no strong peaks observed in the local *Nu-x* plot. The peaks are consistently lower than for the offset electrode counterparts, which leads to a lower HR for any given l_x.

3.6. *Effects of friction parameter and Reynolds number on heat transfer*

This section reports the influence of magnetic field strength (quantified by friction parameter H) and Reynolds number. Other parameters are fixed at $I = 30$, $\omega_f = 1.75$, $\tau/T = 0.25$, $G/d = 2$. The results are shown in figure 20 for $200 \leqslant H \leqslant 5000$ and $Re_L = 1500$ and 3000. The figure shows that for a given Reynolds number, the enhancement in heat transfer due to the imposed current exhibits a non-monotonic relation with friction parameter. At low H, HR increases with increasing H and reaches a peak, before decreasing steadily with further increases in H and eventually reaching an asymptotic value.

This observation is attributed to the competition between inertia and Hartmann damping, i.e. $(a^2/nL^2)Re_L/Ha$ (Sommeria 1986). In the low-H regime, the inertially shed and electrically driven vortices dominate over the damping force, which results in shed vortices being sustained to greater downstream distances. There is a consistently strong interaction between the heated wall and the cylinder wake along the duct, visible in the vorticity field plot in figure 21(*a*). Consequently, the enhancement in the local Nusselt number is nearly uniform throughout the domain (as shown

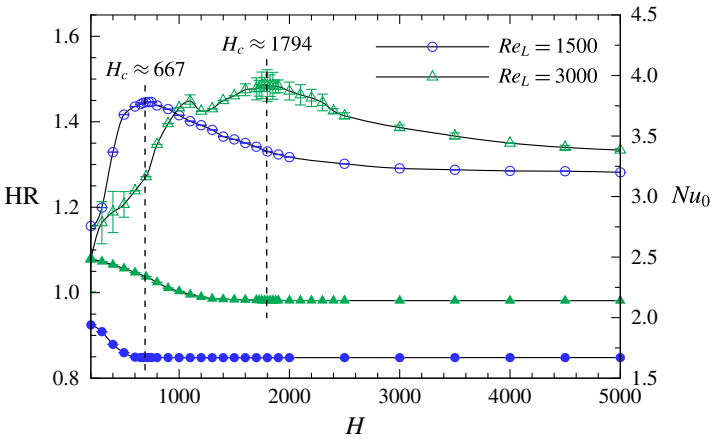

FIGURE 20. (Colour online) (Primary vertical axis) heat transfer enhancement ratio and (secondary vertical axis) base flows time-averaged Nusselt number plotted against friction parameter H for Reynolds numbers $Re_L = 1500$ and 3000. Open symbols represent HR and solid symbols represent Nu_0. The dashed lines indicate a critical value of the friction parameter, above which the cylinder vortex shedding is completely suppressed.

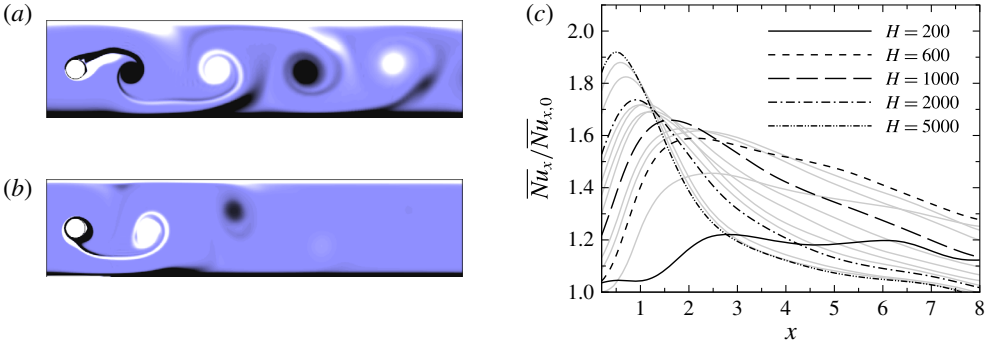

FIGURE 21. (Colour online) (*a*,*b*) Instantaneous vorticity contour plots for $Re_L = 1500$ and (*a*) $H = 300$ and (*b*) $H = 1500$. Contour levels are as per figure 5. (*c*) Normalized time-averaged local Nusselt number along the downstream of the heated wall for $Re_L = 1500$ and H as indicated.

by the almost horizontal curve for $H = 200$ in figure 21(*c*). In the high-H regime, however, Hartmann damping dominates over the driving force. The strength of the shed vortices is relatively high in the near wake due to the strong interaction between the magnetic field and the imposed current forcing, but is damped rapidly after they are shed (as indicated in the plot of vorticity contour in figure 21(*b*). As a result, the strong wake–boundary layer interaction occurs only in the near-wake region, which is reflected by the strong peak of local Nusselt number in the vicinity of the cylinder, followed by a rapid decline further downstream (as shown in figure 21(*b*) for friction parameters in the high-H regime). With H increasing further, the flow field is dominated by the forcing current. However, due to very strong damping, the shedding is completely suppressed and the heat transfer eventually becomes asymptotically independent of H.

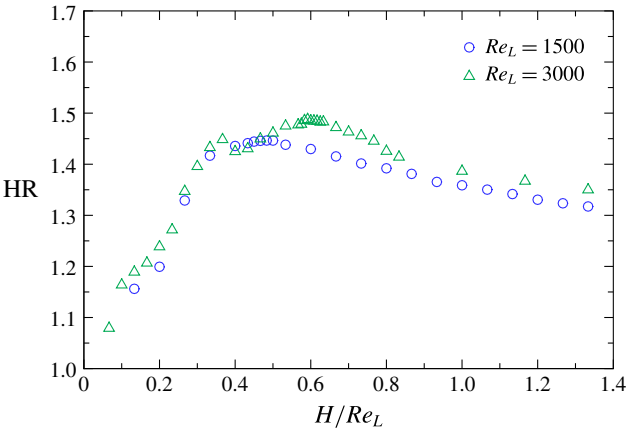

FIGURE 22. (Colour online) Heat transfer enhancement ratio and plotted against H/Re_L for Re_L as indicated. Circle and delta symbols represent $Re_L = 1500$ and 3000, respectively.

HR reaches its maximum value at a friction parameter close to the critical value H_c at which a transition between time-dependent and steady state flows occurs in the base flows. The Nusselt number for the base flows, however, reaches an asymptote beyond the critical friction parameter due to laminarisation (as can be seen in figure 20). This observation is in contrast to cases where the duct walls are conducting, where Nu increased with increasing Ha due to high velocity gradient near the heated wall (Cuevas *et al.* 1997; Takahashi *et al.* 1998). Furthermore, the flow with higher Re_L reached a higher asymptote in the steady state regime due to the increased level of turbulence, which is favourable for effective heat dissipation (Sukoriansky *et al.* 1989). The value of H_c was refined by means of a Stuart–Landau analysis, which while primarily being a tool for analysing the nonlinear futures of an evolving instability, is also convenient for recovering the exponential growth or decay rate for an instability in its linear regime (further details concerning this analysis technique can be found in Hussam, Thompson & Sheard (2011)). Noting the Hartmann friction term in (2.4), the heat transfer enhancement ratio is plotted against H/Re_L, as shown in figure 22. The figure shows that the HR data for both Reynolds numbers nearly collapses into a single curve, suggesting that the enhancement of heat transfer is governed by the H/Re_L. This observation is perhaps not surprising, given that the stability (Sommeria 1986) and the decay of vortices (Sommeria 1988; Hamid *et al.* 2015) in quasi-two-dimensional MHD duct flows are controlled by the H/Re_L parameter.

4. Power and efficiency analysis

In this section, the characteristics of pumping power requirement (expressed in terms of pressure penalty ratio), overall system efficiency resulting from the employment of current injection as a turbulence enhancer and the current injection power input are reported. The pressure penalty ratio PR in this study is the ratio of pressure drop across identical ducts with and without current injection. Inspection of PR across all cases in this study (not shown for brevity) reveals that the pressure drop induced by the imposed current injection is almost negligible, with the maximum pressure increment of 13 % (i.e. $\mathrm{PR}_{max} = 1.13$). It was also observed that the position of the electrode and magnetic field strength have almost no effect on PR, where the

mean (and standard deviation in parentheses) of PR for various investigated electrode positions and Hartmann numbers are respectively 1.004 (0.0032) and 1.012 (0.0067). Furthermore, it was found that cases with the cylinder at the duct centreline show a relatively higher increment in pressure drop as compared to the cases with an offset cylinder, and becomes more apparent at a higher current amplitude. In some cases, the imposed current injection has a desirable effect by reducing the pressure drop with respect to the base cases, with a maximum reduction of 4 % (i.e. $\mathrm{PR}_{min} = 0.96$). Since PR is almost unity for all cases, it follows then that the system efficiency (quantified by the efficiency index η as in (2.11)) and the heat transfer enhancement ratio HR have a similar dependency on all varying parameters (as presented in the previous sections). The maximum efficiency index was found to be $\eta = 1.91$ for the case with highest current amplitude, which produces the highest heat transfer enhancement ratio of HR = 1.89. This enhancement in heat transfer is 55 % more than what has been reported for rotationally oscillating cylinder rotating at maximum amplitude and optimum frequency (i.e. HR $\approx$ 1.22) (Hussam *et al.* 2012*a*). In the hydrodynamic counterpart, maximum enhancement of HR $\approx$ 1.55 has been reported when the cylinder with $\beta = 1/3$ rotationally oscillates with maximum amplitude and within the lock-in regime (Beskok *et al.* 2012).

It is important to mention that the effect of inertially driven recirculation in the parallel planes on the heat transfer is assumed to be negligible in the present work. Recent investigation by Baker, Pothérat & Davoust (2015) has shown that in the limit of quasi-2-D base flow, the local fluid rotation above the Hartmann layer induces secondary counter-rotating 3-D recirculations which correspond to Ekman pumping. The emergence of these recirculations drives an inward radial flow within the Hartmann layers, and thus can potentially transport a fraction of heat towards the core flow and alter the heat transfer characteristics of the flow. However, it has been reported (Alboussière, Uspenski & Moreau 1999) that the 3-D recirculation is weakened under a strong magnetic field. It is then anticipated that this weak recirculation becomes less effective in transferring heat relative to the primary vortex flow, justifying the aforementioned assumption.

The average power supply due to current injection is proportional to I_{rms}^2, where I_{rms} is the root mean square of injected current. Since the dimensional current amplitude

$$\hat{I} = IaU_0\sqrt{\rho\nu\sigma} = 2\alpha\sqrt{\rho\nu^3\sigma}IRe_L, \tag{4.1}$$

and taking the properties of a low melting point eutectic alloy $\mathrm{Ga}^{68}\mathrm{In}^{20}\mathrm{Sn}^{12}$ at 20 °C (as presented in § 2.2) and $\alpha = 1$, the dimensional current injection amplitude is given by

$$\hat{I} \approx 5.96 \times 10^{-5} IRe_L \,\mathrm{A}. \tag{4.2}$$

In the present investigation, the bulk of the numerical simulations were based on the flow Reynolds number $Re_L = 1500$, while the dimensionless current injection amplitude was varied between 6 and 90, this then corresponds to a dimensional current of $\hat{I} \approx 0.5$ and 8 A, respectively. For the sake of comparison, this current supply is three orders of magnitude lower than that required to induce the confining magnetic fields for fusion blanket MHD research in the MEKKA experimental facility (Barleon, Mack & Stieglitz 1996). The use of electrically generated quasi-two-dimensional vortices for heat transfer augmentation therefore appears to be viable, at least in principle. There are, however, significant technical challenges in realizing controlled current injection

through electrodes that are embedded in a Hartmann wall. These include ensuring good contact between the electrode surface and the liquid metal, as poor contact can lead to overheating, and the effect on the fluid rotation above the electrode may be significant. Furthermore, the electrode–liquid metal interface is also susceptible to varying resistance, where erratic variation in contact resistance can lead to an irregular electric current distribution over multiple electrodes. This effect can be avoided by incorporating ohmic resistance of orders of magnitudes higher than any other resistance in electric circuit of each electrode (Pothérat & Klein 2014). This solution would, however, result in energy consumption significantly higher than previously estimated. Furthermore, it has been shown previously that the electrical resistance increases monotonically with increasing imposed magnetic field (Sommeria 1988). The technological challenges toward implementation of such system are outside the scope of the present study.

5. Conclusions

The present study has investigated the characteristics of electrically generated quasi-two-dimensional vortices to enhance sidewall heat transfer in MHD ducts containing a circular cylinder vortex promoter under a strong transverse magnetic field. A solution to the current injection forcing field was first derived for a domain extending infinitely in streamwise direction and bounded by duct sidewalls, and was imposed as a forcing field in simulations of the quasi-two-dimensional flows. It was found that the heat transfer enhancement are closely associated with the resulting wake dynamics and their interactions with the heated wall. The results indicate a maximum Nusselt number improvement of about 90 % for ducts with current injection, and is highly dependent on the imposed forcing current parameters. Non-monotonic relationships between the heat transfer enhancement ratio HR and the forcing frequency and magnetic field strength were observed. The HR, however, increased almost linearly with forcing amplitude and pulse width. It is also significantly influenced by the electrode position in the transverse direction.

An examination of the local Nusselt number variation along the duct revealed a general trend wherein a sudden jump were followed by an abrupt decrease in the local Nu, due to the deflection of the wake vortices away from the heated wall. In some cases, the appearance of secondary peak in the local Nusselt number plots has a significant contribution to the overall heat transfer enhancement. Despite the different mechanism of vortex generation in the present MHD duct flow, the heat transfer enhancement exhibits similar characteristics to the hydrodynamic counterpart, whereby the local Nusselt number distribution is closely associated with the strength of the wake–boundary layer interaction and the entrainment of fluid from the boundary layer into the wake. The factors determining the interaction and entrainment are the size, pattern/mode and frequency of shedding of the wake vortex.

Spectral analysis of the cylinder lift coefficient revealed broadening of lock-in regime with increasing forcing amplitude. The analysis also revealed a distinct spectrum of cylinder lift coefficient in the unlock-in regime. Nonlinear coupling of the cylinder vortex shedding with the forcing current injection can account for distinct spectral peaks beyond the lock-in regime.

The analysis of the pressure drop indicates that the employment of current injection as turbuliser does not significantly alter the hydraulic losses. This yields an efficiency index ranging between 97 % and 191 %.

Acknowledgements

This research was supported by the Australian Research Council through Discovery grants DP120100153 and DP150102920, a high-performance computing time allocations from the National Computational Infrastructure (NCI), which is supported by the Australian Government, and the Monash SunGRID. The authors are grateful to Professor A. Pothérat, Coventry University, for helpful discussions and advice, and also thank the anonymous referees for their productive comments and suggestions. A.H.A.H. is supported by the Malaysia Ministry of Education and the Universiti Teknologi MARA, Malaysia.

Appendix A

In (2.4), the non-dimensional forcing velocity field $\boldsymbol{u}_0$ is defined as

$$\boldsymbol{u}_0 = \boldsymbol{j} \times \boldsymbol{e}_z = \nabla\psi_0 \times \boldsymbol{e}_z, \tag{A 1}$$

where $\boldsymbol{j}$ is the electric current density, $\boldsymbol{e}_z$ is the unit vector in the z-direction and ψ_0 is the electrical potential. The electric current density and the electrical potential are scaled by $\sigma BU_0/Ha = U_0\sqrt{\rho\nu\sigma}/a$ and aBU_0, respectively. In a high magnetic field application, the change in the field due to the currents induced by the flow can be neglected. Under this condition, the equations governing continuity of electric current and incompressibility are also linear, so they may be averaged to give $\nabla \cdot \boldsymbol{j} = -j_w$, $\boldsymbol{j} = Ha(\boldsymbol{E} + \boldsymbol{u} \times \boldsymbol{e}_z)$ and $\nabla \cdot \boldsymbol{u} = 0$. Here j_w is the current density injected at one or both of the confining planes, and $\boldsymbol{E}$ is a dimensionless electrical field. The z-averaged current can be expressed as the gradient of a scalar field ψ_0 satisfying a Poisson equation with the source term being j_w, i.e. $\boldsymbol{j} = \nabla\psi_0$, obtained from $\nabla^2\psi_0 = -j_w$ (Pothérat *et al.* 2005). This Poisson equation is first solved (Polyanin 2001) for a source term at the current injection point that is a Dirac function located at $(0, l_y)$, i.e. $j_w(x, y) = I\delta(x, y - l_y)$, on a domain extending infinitely in streamwise direction and bounded by duct sidewalls at $y = \pm 1$. Physically, the current circuit would be completed far upstream and downstream of the electrode. Imposing zero Neumann conditions on the electrical potential field at the boundaries due to the insulating Shercliff walls (Pothérat *et al.* 2000), i.e. $\partial\psi_0/\partial y = 0$ at $y = \pm 1$, leads to

$$\begin{aligned}\psi_0(x, y) \;=\; & \frac{I}{4\pi}\left[\log\left(\frac{1}{\cosh(\pi x/2) - \cos[\pi(y + 1 + l_y)/2]}\right)\right. \\ & \left. + \log\left(\frac{1}{\cosh(\pi x/2) - \cos[\pi(y + 1 - l_y)/2]}\right)\right].\end{aligned} \tag{A 2}$$

I is the non-dimensional current amplitude, which is defined as

$$I = \frac{\hat{I}}{aU_0\sqrt{\rho\nu\sigma}}. \tag{A 3}$$

Substituting (A 2) into (A 1), the forcing velocity field becomes

$$\boldsymbol{u}_0 = \nabla\psi_0 \times \boldsymbol{e}_z = \left\langle \frac{\partial\psi_0}{\partial x}, \frac{\partial\psi_0}{\partial y}, 0 \right\rangle \times \boldsymbol{e}_z. \tag{A 4}$$

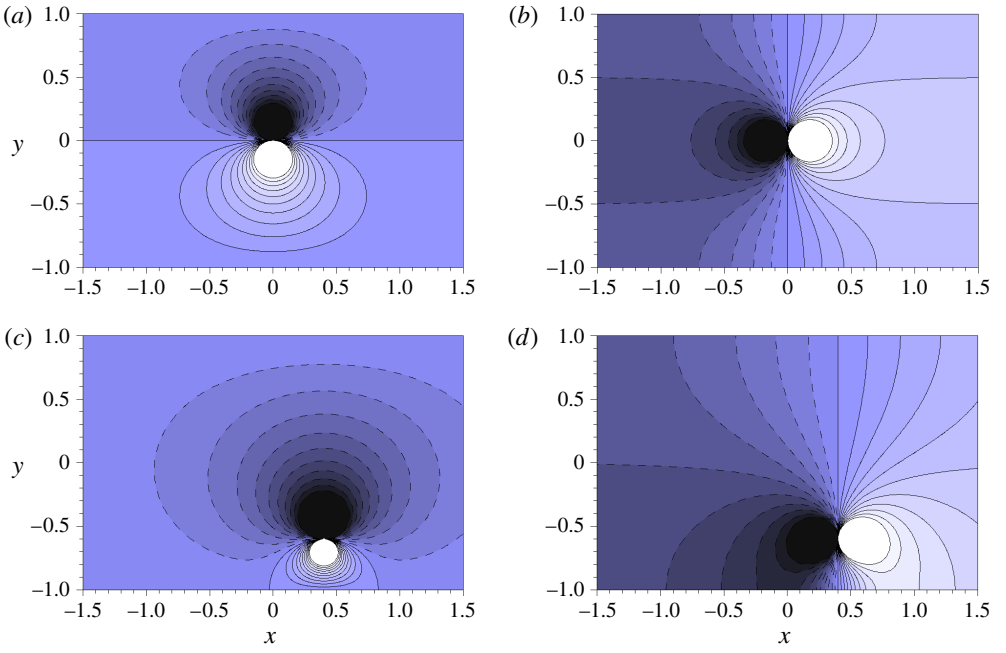

FIGURE 23. (Colour online) Contour plots of the horizontal (*a*,*c*) and vertical (*b*,*d*) components of $\boldsymbol{u}_0$ for $I = 60$, $H = 500$, $Re_L = 1500$ and electrode locations (*a*,*b*) $(x, y) = (0, 0)$ and (*c*,*d*) $(x, y) = (0.4, -0.6)$. Contour levels range between -5 and 5, with light and dark contours representing positive and negative velocity, respectively.

Evaluating (A 4) for electrode positioned at $(l_x,\ 1 - l_y)$ yields $\boldsymbol{u}_0$ components

$$u_0 = \frac{I}{8}\left(\frac{\sin[\pi(y+1+l_y)/2]}{\cos[\pi(y+1+l_y)/2] - \cosh[\pi(x-l_x)/2]} + \frac{\sin[\pi(y+1-l_y)/2]}{\cos[\pi(y+1-l_y)/2] - \cosh[\pi(x-l_x)/2]}\right), \tag{A 5}$$

and

$$v_0 = \frac{I}{8}\left(-\frac{\sinh[\pi(x-l_x)/2]}{\cos[\pi(y+1+l_y)/2] - \cosh[\pi(x-l_x)/2]} - \frac{\sinh[\pi(x-l_x)/2]}{\cos[\pi(y+1-l_y)/2] - \cosh[\pi(x-l_x)/2]}\right). \tag{A 6}$$

The contours of the resulting horizontal and vertical components of the forcing velocity fields for $I = 60$, $H = 500$ and $Re_L = 1500$ are depicted in figure 23. Unless otherwise mentioned, the current injection amplitude is expressed non-dimensionally throughout the paper as in (A 3).

In the present investigation, the current is either injected from the base of the cylinder or from an electrode located away from the cylinder. In the former arrangement, the physical realisation of this set-up is likely from a ring of electrodes around the base of the cylinder (as depicted in figure 24). In the limit of high

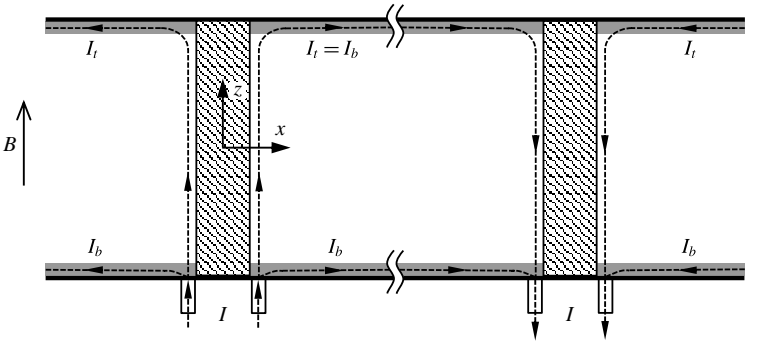

FIGURE 24. Schematic representation of the electric current paths (dotted lines) from a ring of electrodes around the base of the cylinder (the cylinder is represented by a diagonal line shading) in the limit of high Hartmann number and interaction parameter. The electrode is embedded into one of the Hartmann walls and made flush with the surface to avoid disturbance of the flow. The Hartmann layers are shaded grey, which contain most of the current paths in for quasi-2-D flow.

Hartmann number and high interaction parameter, most of the electric current flow is through the Hartmann layers (Pothérat & Klein 2014). The currents are equally divided into each Hartmann layer (i.e. $I_t = I_b$, where subscripts t and b correspond to top and bottom, respectively), which results in an axisymmetric two-dimensional vortex in the core flow. The current also interacts with the Shercliff layer only within the very thin top and bottom Hartmann layers. It is anticipated that such an interaction to be relatively insignificant to affect the core flow and thus neglected in the present formulation. For a thorough description of electric current path in the latter arrangement, the reader is referred to Pothérat & Klein (2014).

REFERENCES

ALBOUSSIÈRE, T., USPENSKI, V. & MOREAU, R. 1999 Quasi-2D MHD turbulent shear layers. *Exp. Therm. Fluid Sci.* **20** (1), 19–24.

ALI, M. S. M., DOOLAN, C. J. & WHEATLEY, V. 2009 Grid convergence study for a two-dimensional simulation of flow around a square cylinder at a low Reynolds number. In *Seventh International Conference on CFD in The Minerals and Process Industries* (ed. P. J. Witt & M. P. Schwarz), pp. 1–6. CSIRO.

BAKER, N. T., POTHÉRAT, A. & DAVOUST, L. 2015 Dimensionality, secondary flows and helicity in low-*Rm* MHD vortices. *J. Fluid Mech.* **779**, 325–350.

BARLEON, L., MACK, K.-J. & STIEGLITZ, R. 1996 The MEKKA-facility a flexible tool to investigate MHD-flow phenomena. *Tech. Rep.* ZKA 5821. Institute of Applied Thermo- and Fluid Dynamics, Research Centre Karlsruhe.

BESKOK, A., RAISEE, M., CELIK, B., YAGIZ, B. & CHERAGHI, M. 2012 Heat transfer enhancement in a straight channel via a rotationally oscillating adiabatic cylinder. *Intl J. Therm. Sci.* **58**, 61–69.

BRANOVER, H., EIDELMAN, A. & NAGORNY, M. 1995 Use of turbulence modification for heat transfer enhancement in liquid metal blankets. *Fusion Engng Des.* **27**, 719–724.

BROUILLETTE, E. C. & LYKOUDIS, P. S. 1967 Magneto-fluid-mechanic channel flow. I. Experiment. *Phys. Fluids* **10** (5), 995–1001.

BÜHLER, L. 1996 Instabilities in quasi-two-dimensional magnetohydrodynamic flows. *J. Fluid Mech.* **326**, 125–150.

BURR, U., BARLEON, L., MÜLLER, U. & TSINOBER, A. 2000 Turbulent transport of momentum and heat in magnetohydrodynamic rectangular duct flow with strong sidewall jets. *J. Fluid Mech.* **406**, 247–279.

CASSELLS, O. G. W., HUSSAM, W. K. & SHEARD, G. J. 2016 Heat transfer enhancement using rectangular vortex promoters in confined quasi-two-dimensional magnetohydrodynamic flows. *Intl J. Heat Mass Transfer* **93**, 186–199.

CELIK, B., AKDAG, U., GUNES, S. & BESKOK, A. 2008 Flow past an oscillating circular cylinder in a channel with an upstream splitter plate. *Phys. Fluids* **20**, 103603.

CELIK, B., RAISEE, M. & BESKOK, A. 2010 Heat transfer enhancement in a slot channel via a transversely oscillating adiabatic circular cylinder. *Intl J. Heat Mass Transfer* **53**, 626–634.

CUEVAS, S., PICOLOGLOU, B. F., WALKER, J. S., TALMAGE, G. & HUA, T. Q. 1997 Heat transfer in laminar and turbulent liquid-metal MHD flows in square ducts with thin conducting or insulating walls. *Intl J. Engng Sci.* **35** (5), 505–514.

DAVIDSON, P. A. 2001 *An Introduction to Magnetohydrodynamics*, vol. 25. Cambridge University Press.

FRANK, M., BARLEON, L. & MÜLLER, U. 2001 Visual analysis of two-dimensional magnetohydrodynamics. *Phys. Fluids* **13**, 2287–2295.

FU, WU-SHUNG & TONG, BAO-HONG 2004 Numerical investigation of heat transfer characteristics of the heated blocks in the channel with a transversely oscillating cylinder. *Intl J. Heat Mass Transfer* **47**, 341–351.

GARDNER, R. A. & LYKOUDIS, P. S. 1971 Magneto-fluid-mechanic pipe flow in a transverse magnetic field Part 2. Heat transfer. *J. Fluid Mech.* **48** (1), 129–141.

GRIFFIN, O. M. & RAMBERG, S. E. 1976 Vortex shedding from a cylinder vibrating in line with an incident uniform flow. *J. Fluid Mech.* **75** (2), 257–271.

HAMID, A. H. A., HUSSAM, W. K., POTHÉRAT, A. & SHEARD, G. J. 2015 Spatial evolution of a quasi-two-dimensional Kármán vortex street subjected to a strong uniform magnetic field. *Phys. Fluids* **27**, 053602.

HARTMANN, J. & LAZARUS, F. 1937 Hg-dynamics II: experimental investigations on the flow of mercury in a homogeneous magnetic field. *Math.-fys. Med.* **15** (7), 1–45.

HUNT, J. C. R. 1965 Magnetohydrodynamic flow in rectangular ducts. *J. Fluid Mech.* **21** (4), 577–590.

HUNT, J. C. R. & MALCOLM, D. G. 1968 Some electrically driven flows in magnetohydrodynamics Part 2. Theory and experiment. *J. Fluid Mech.* **33** (04), 775–801.

HUSSAM, W. K. & SHEARD, G. J. 2013 Heat transfer in a high Hartmann number MHD duct flow with a circular cylinder placed near the heated side-wall. *Intl J. Heat Mass Transfer* **67**, 944–954.

HUSSAM, W. K., THOMPSON, M. C. & SHEARD, G. J. 2011 Dynamics and heat transfer in a quasi-two-dimensional MHD flow past a circular cylinder in a duct at high Hartmann number. *Intl J. Heat Mass Transfer* **54**, 1091–1100.

HUSSAM, W. K., THOMPSON, M. C. & SHEARD, G. J. 2012*a* Enhancing heat transfer in a high Hartmann number magnetohydrodynamic channel flow via torsional oscillation of a cylindrical obstacle. *Phys. Fluids* **24**, 113601.

HUSSAM, W. K., THOMPSON, M. C. & SHEARD, G. J. 2012*b* Optimal transient disturbances behind a circular cylinder in a quasi-two-dimensional magnetohydrodynamic duct flow. *Phys. Fluids* **24**, 024105.

KANARIS, N., ALBETS, X., GRIGORIADIS, D. & KASSINOS, S. 2013 Three-dimensional numerical simulations of magnetohydrodynamic flow around a confined circular cylinder under low, moderate, and strong magnetic fields. *Phys. Fluids* **25**, 074102.

KARNIADAKIS, G. E. & TRIANTAFYLLOU, G. S. 1989 Frequency selection and asymptotic states in laminar wakes. *J. Fluid Mech.* **199**, 441–469.

KIEFT, R. N., RINDT, C. C. M., VAN STEENHOVEN, A. A. & VAN HEIJST, G. J. F. 2003 On the wake structure behind a heated horizontal cylinder in cross-flow. *J. Fluid Mech.* **486**, 189–211.

KLEIN, R., POTHÉRAT, A. & ALFERENOK, A. 2009 Experiment on a confined electrically driven vortex pair. *Phys. Rev.* E **79**, 016304.

KOLESNIKOV, Y. B. & ANDREEV, O. V. 1997 Heat-transfer intensification promoted by vortical structures in closed channel under magnetic field. *Exp. Therm. Fluid Sci.* **15**, 82–90.

KOOPMANN, G. H. 1967 The vortex wakes of vibrating cylinders at low Reynolds numbers. *J. Fluid Mech.* **28** (3), 501–512.

KRASNOV, D., ZIKANOV, O. & BOECK, T. 2012 Numerical study of magnetohydrodynamic duct flow at high Reynolds and Hartmann numbers. *J. Fluid Mech.* **704**, 421–446.

LAHJOMRI, J., CAPÉRAN, PH. & ALEMANY, A. 1993 The cylinder wake in a magnetic field aligned with the velocity. *J. Fluid Mech.* **253**, 421–448.

LAM, K. M. 2009 Vortex shedding flow behind a slowly rotating circular cylinder. *J. Fluids Struct.* **25**, 245–262.

LUNDQUIST, S. 1949 Experimental investigations of magneto-hydrodynamic waves. *Phys. Rev.* **76** (12), 1805–1809.

LYON, R. N. 1952 *Liquid-Metals Handbook*, 2nd edn. Navexos P-733.

MAHFOUZ, F. M. & BADR, H. M. 2000 Forced convection from a rotationally oscillating cylinder placed in a uniform stream. *Intl J. Heat Mass Transfer* **43**, 3093–3104.

MALANG, S. & TILLACK, M. S. 1995 Development of self-cooled liquid metal breeder blankets. *Tech. Rep.* FZKA 5581. Forschungszentrum Karlsruhe GmbH Karlsruhe.

MIYAZAKI, K., INOUE, H., KIMOTO, T., YAMASHITA, S., INOUE, S. & YAMAOKA, N. 1986 Heat transfer and temperature fluctuation of lithium flowing under transverse magnetic field. *J. Nucl. Sci. Technol.* **23** (7), 582–593.

MOLOKOV, S. 1994 Liquid metal flows in manifolds and expansions of insulating rectangular ducts in the plane perpendicular to a strong magnetic field. *Tech. Rep.* KfK 5272. Kernforschungszentrum Karlsruhe GmbH Karlsruhe.

MORLEY, N. B., BURRIS, J., CADWALLADER, L. C. & NORNBERG, M. D. 2008 GaInSn usage in the research laboratory. *Rev. Sci. Instrum.* **79**, 056107.

MÜCK, B., GÜNTHER, C., MÜLLER, U. & BÜHLER, L. 2000 Three-dimensional MHD flows in rectangular ducts with internal obstacles. *J. Fluid Mech.* **418** (1), 265–295.

MÜLLER, U. & BÜHLER, L. 2001 *Magnetofluiddynamics in Channels and Containers*. Springer.

NEILD, A., NG, T. W., SHEARD, G. J., POWERS, M. & OBERTI, S. 2010 Swirl mixing at microfluidic junctions due to low frequency side channel fluidic perturbations. *Sensors Actuators* **150**, 811–818.

POLYANIN, A. D. 2001 *Handbook of Linear Partial Differential Equations for Engineers and Scientists*. Chapman & Hall/CRC.

POTHÉRAT, A. 2007 Quasi-two-dimensional perturbations in duct flows under transverse magnetic field. *Phys. Fluids* **19**, 074104.

POTHÉRAT, A. & KLEIN, R. 2014 Why, how and when MHD turbulence at low *Rm* becomes three-dimensional. *J. Fluid Mech.* **761**, 168–205.

POTHÉRAT, A. & KORNET, K. 2015 The decay of wall-bounded MHD turbulence at low. *J. Fluid Mech.* **783**, 605–636.

POTHÉRAT, A. & SCHWEITZER, J.-P. 2011 A shallow water model for magnetohydrodynamic flows with turbulent Hartmann layers. *Phys. Fluids* **23** (5), 055108.

POTHÉRAT, A., SOMMERIA, J. & MOREAU, R. 2000 An effective two-dimensional model for MHD flows with transverse magnetic field. *J. Fluid Mech.* **424**, 75–100.

POTHÉRAT, A., SOMMERIA, J. & MOREAU, R. 2002 Effective boundary conditions for magnetohydrodynamic flows with thin Hartmann layers. *Phys. Fluids* **14**, 403–410.

POTHÉRAT, A., SOMMERIA, J. & MOREAU, R. 2005 Numerical simulations of an effective two-dimensional model for flows with a transverse magnetic field. *J. Fluid Mech.* **534**, 115–143.

RHOADS, J. R., EDLUND, E. M. & JI, H. 2014 Effects of magnetic field on the turbulent wake of a cylinder in free-surface magnetohydrodynamic channel flow. *J. Fluid Mech.* **742**, 446–465.

ROBERTS, P. H. 1967 *An Introduction to Magnetohydrodynamics*. Longmans.

SHATROV, V. & GERBETH, G. 2010 Marginal turbulent magnetohydrodynamic flow in a square duct. *Phys. Fluids* **22** (8), 084101.

SHEARD, G. J. 2011 Wake stability features behind a square cylinder: focus on small incidence angles. *J. Fluids Struct.* **27**, 734–742.

SHERCLIFF, J. A. 1953 Steady motion of conducting fluids in pipes under transverse magnetic fields. *Math. Proc. Cambridge* **49**, 136–144.

SMOLENTSEV, S & MOREAU, R 2007 One-equation model for quasi-two-dimensional turbulent magnetohydrodynamic flows. *Phys. Fluids* **19**, 078101.

SMOLENTSEV, S., VETCHA, N. & MOREAU, R. 2012 Study of instabilities and transitions for a family of quasi-two-dimensional magnetohydrodynamic flows based on a parametrical model. *Phys. Fluids* **24**, 024101.

SMOLENTSEV, S., WONG, C., MALANG, S., DAGHER, M. & ABDOU, M. 2010 MHD considerations for the DCLL inboard blanket and access ducts. *Fusion Engng Des.* **85** (7), 1007–1011.

SOMMERIA, J. 1986 Experimental study of the two-dimensional inverse energy cascade in a square box. *J. Fluid Mech.* **170**, 139–168.

SOMMERIA, J. 1988 Electrically driven vortices in a strong magnetic field. *J. Fluid Mech.* **189**, 553–569.

SOMMERIA, J. & MOREAU, R. 1982 Why, how, and when, MHD turbulence becomes two-dimensional. *J. Fluid Mech.* **118**, 507–518.

SUKORIANSKY, S., KLAIMAN, D., BRANOVER, H. & GREENSPAN, E. 1989 MHD enhancement of heat transfer and its relevance to fusion reactor blanket design. *Fusion Engng Des.* **8**, 277–282.

TAKAHASHI, M., ARITOMI, M., INOUE, A. & MATSUZAKI, M. 1998 MHD pressure drop and heat transfer of lithium single-phase flow in a rectangular channel under transverse magnetic field. *Fusion Engng Des.* **42**, 365–372.

WALSH, M. J. & WEINSTEIN, L. M. 1979 Drag and heat-transfer characteristics of small longitudinally ribbed surfaces. *AIAA J.* **17** (7), 770–771.

YANG, S.-J. 2003 Numerical study of heat transfer enhancement in a channel flow using an oscillating vortex generator. *Heat Mass Transfer* **39**, 257–265.